The Astrophysical Journal Letters, 949:L25 (18pp), 2023 June 1 https://doi.org/10.3847/2041-8213/acd2d9

CEERS Spectroscopic Confirmation of NIRCam-selected $z \gtrsim 8$ Galaxy Candidates with JWST/NIRSpec: Initial Characterization of Their Properties

Seiji Fujimoto[1,28], Pablo Arrabal Haro[2], Mark Dickinson[2], Steven L. Finkelstein[1], Jeyhan S. Kartaltepe[3], Rebecca L. Larson[1,29], Denis Burgarella[4], Micaela B. Bagley[1], Peter Behroozi[5,6], Katherine Chworowsky[1,29], Michaela Hirschmann[7,8], Jonathan R. Trump[9], Stephen M. Wilkins[10,11], L. Y. Aaron Yung[12,30], Anton M. Koekemoer[13], Casey Papovich[14,15], Nor Pirzkal[16], Henry C. Ferguson[13], Adriano Fontana[17], Norman A. Grogin[13], Andrea Grazian[18], Lisa J. Kewley[19], Dale D. Kocevski[20], Jennifer M. Lotz[21], Laura Pentericci[17], Swara Ravindranath[13], Rachel S. Somerville[22], Stephen M. Wilkins[10,11], Ricardo O. Amorín[23,24], Bren E. Backhaus[9], Antonello Calabrò[17], Caitlin M. Casey[1], M. C. Cooper[25], Vital Fernández[24], Maximilien Franco[1], Mauro Giavalisco[26], Nimish P. Hathi[13], Santosh Harish[3], Taylor A. Hutchison[12,30], Kartheik G. Iyer[27], Intae Jung[13], Ray A. Lucas[13], and Jorge A. Zavala[6]

[1] Department of Astronomy, The University of Texas at Austin, Austin, TX, USA; fujimoto@utexas.edu
[2] NSF's National Optical-Infrared Astronomy Research Laboratory, 950 N. Cherry Ave., Tucson, AZ 85719, USA
[3] Laboratory for Multiwavelength Astrophysics, School of Physics and Astronomy, Rochester Institute of Technology, 84 Lomb Memorial Drive, Rochester, NY 14623, USA
[4] Aix Marseille Univ, CNRS, CNES, LAM Marseille, France
[5] Department of Astronomy and Steward Observatory, University of Arizona, Tucson, AZ 85721, USA
[6] Division of Science, National Astronomical Observatory of Japan, 2-21-1 Osawa, Mitaka, Tokyo 181-8588, Japan
[7] Institute for Physics, Laboratory for Galaxy Evolution and Spectral modelling, Ecole Polytechnique Federale de Lausanne, Observatoire de Sauverny, Chemin Pegasi 51, 1290 Versoix, Switzerland
[8] INAF, Osservatorio Astronomico di Trieste, Via Tiepolo 11, I-34131 Trieste, Italy
[9] Department of Physics, 196 Auditorium Road, Unit 3046, University of Connecticut, Storrs, CT 06269, USA
[10] Astronomy Centre, University of Sussex, Falmer, Brighton BN1 9QH, UK
[11] Institute of Space Sciences and Astronomy, University of Malta, Msida MSD 2080, Malta
[12] Astrophysics Science Division, NASA Goddard Space Flight Center, 8800 Greenbelt Rd, Greenbelt, MD 20771, USA
[13] Space Telescope Science Institute, 3700 San Martin Drive, Baltimore, MD 21218, USA
[14] Department of Physics and Astronomy, Texas A&M University, College Station, TX, 77843-4242 USA
[15] George P. and Cynthia Woods Mitchell Institute for Fundamental Physics and Astronomy, Texas A&M University, College Station, TX, 77843-4242 USA
[16] ESA/AURA Space Telescope Science Institute, 3700, San Martin Drive, MD 21218, USA
[17] INAF Osservatorio Astronomico di Roma, Via Frascati 33, I-00078 Monte Porzio Catone, Rome, Italy
[18] INAF–Osservatorio Astronomico di Padova, Vicolo dell'Osservatorio 5, I-35122, Padova, Italy
[19] Harvard-Smithsonian Center for Astrophysics, 60 Garden Street, Cambridge, MA 02138, USA
[20] Department of Physics and Astronomy, Colby College, Waterville, ME 04901, USA
[21] Gemini Observatory/NSF's National Optical-Infrared Astronomy Research Laboratory, 950 N. Cherry Ave., Tucson, AZ 85719, USA
[22] Center for Computational Astrophysics, Flatiron Institute, 162 5th Avenue, New York, NY 10010, USA
[23] Instituto de Investigación Multidisciplinar en Ciencia y Tecnología, Universidad de La Serena, Raul Bitrán 1305, La Serena 2204000, Chile
[24] Departamento de Astronomía, Universidad de La Serena, Av. Juan Cisternas 1200 Norte, La Serena 1720236, Chile
[25] Department of Physics & Astronomy, University of California, Irvine, 4129 Reines Hall, Irvine, CA 92697, USA
[26] University of Massachusetts Amherst, 710 North Pleasant Street, Amherst, MA 01003-9305, USA
[27] Dunlap Institute for Astronomy & Astrophysics, University of Toronto, Toronto, ON M5S 3H4, Canada

Received 2023 January 22; revised 2023 May 2; accepted 2023 May 3; published 2023 June 5

Abstract

We present JWST NIRSpec spectroscopy for 11 galaxy candidates with photometric redshifts of $z \simeq 9-13$ and $M_{\rm UV} \in [-21, -18]$ newly identified in NIRCam images in the Cosmic Evolution Early Release Science Survey. We confirm emission line redshifts for 7 galaxies at $z = 7.762$–8.998 using spectra at $\sim$1–5 μm either with the NIRSpec prism or its three medium-resolution ($R \sim 1000$) gratings. For $z \simeq 9$ photometric candidates, we achieve a high confirmation rate of $\simeq$90%, which validates the classical dropout selection from NIRCam photometry. No robust emission lines are identified in three galaxy candidates at $z > 10$, where the strong [O III] and Hβ lines would be redshifted beyond the wavelength range observed by NIRSpec, and the Lyα continuum break is not detected with the sensitivity of the current data. Compared with Hubble Space Telescope-selected bright galaxies ($M_{\rm UV} \simeq -22$) that are similarly spectroscopically confirmed at $z \simeq 8-9$, these NIRCam-selected galaxies are characterized by lower star formation rates (SFRs; SFR $\simeq 4\,M_\odot$ yr^{-1}) and lower stellar masses ($\simeq 10^8\,M_\odot$), but with higher specific SFR ($\simeq$40 Gyr^{-1}), higher [O III]+Hβ equivalent widths ($\simeq$1100 Å), and elevated production

---

[28] Hubble Fellow.
[29] NSF Graduate Fellow.
[30] NASA Postdoctoral Fellow.

efficiency of ionizing photons ($\log(\xi_{\rm ion}/{\rm Hz\ erg^{-1}}) \simeq 25.8$) induced by young stellar populations (<10 Myr) accounting for ≃20% of the galaxy mass, highlighting the key contribution of faint galaxies to cosmic reionization. Taking advantage of the homogeneous selection and sensitivity, we also investigate metallicity and ISM conditions with empirical calibrations using the $[{\rm O\,III}]_{5008}/{\rm H}\beta$ ratio. We find that galaxies at $z \simeq 8-9$ have higher SFRs and lower metallicities than galaxies at similar stellar masses at $z \simeq 2-6$, which is generally consistent with the current galaxy formation and evolution models.

Unified Astronomy Thesaurus concepts: Early universe (435); Galaxy formation (595); Galaxy evolution (594); High-redshift galaxies (734)

1. Introduction

Studying early galaxies is key to understanding fundamental cosmological questions such as the development of large-scale structure, dark matter, and the processes that govern cosmic reionization and early galaxy formation and evolution. In the last decades, the search for galaxies seen within the epoch of reionization has been successful at $6 \lesssim z \lesssim 11$. With thousands of galaxies discovered, deep Hubble Space Telescope (HST) surveys have provided valuable demographic data for these galaxies, including an initial characterization of the stellar component, in terms of unobscured star formation rates (SFRs) and sizes (e.g., Ellis et al. 2013; Bouwens et al. 2015; Finkelstein et al. 2015; Oesch et al. 2016; Bhatawdekar et al. 2019).

The start of JWST operations (Rigby et al. 2023) has led to significant progress in the discovery and investigation of galaxies at very early cosmic epochs. From the Early Release Observations (Pontoppidan et al. 2022) and the Early Release Science (ERS; e.g., Treu et al. 2022; Finkelstein et al. 2023) programs, multiple NIRCam imaging surveys have been carried out toward both lensing clusters and blank fields, where dozens of high-redshift galaxy candidates have been identified at $z \simeq 9$–17 (e.g., Adams et al. 2023; Atek et al. 2023; Bouwens et al. 2023b; Bradley et al. 2022; Castellano et al. 2022; Finkelstein et al. 2022, 2023; Labbe et al. 2023; Morishita & Stiavelli 2023; Naidu et al. 2022c; Yan et al. 2023; Donnan et al. 2023a; Harikane et al. 2023b). Their abundance at the bright-end ($M_{\rm UV} \lesssim -20$) exceeds nearly all theoretical predictions so far (e.g., Behroozi & Silk 2015; Dayal et al. 2017; Behroozi et al. 2019, 2020; Davé et al. 2019; Yung et al. 2019a, 2020a; Kannan et al. 2022; Mason et al. 2023; Wilkins et al. 2023, 2022), suggesting several possibilities, including that the star formation in early systems is dominated by a top-heavy initial mass function (IMF), complete lack of dust attenuation, and/or changing star formation physics (e.g., Boylan-Kolchin 2023; Ferrara et al. 2023; Lovell et al. 2023; Menci et al. 2022; Finkelstein et al. 2023; Harikane et al. 2023b).

Deep Atacama Large Millimeter/submillimeter Array (ALMA) follow-up observations have been immediately performed through the Director's Discretionary Time for several remarkably bright ($M_{\rm UV} \in [-22, -21]$) JWST galaxy candidates at $z \sim 11$–17 (e.g., Castellano et al. 2022; Naidu et al. 2022c; Harikane et al. 2023b), showing no robust dust continuum detection from any of these candidates (Bakx et al. 2023; Fujimoto et al. 2022a; Yoon et al. 2022). These ALMA results disfavor the possibility of lower-z dusty interlopers (Fujimoto et al. 2022a) and show possible [O III] line detection (Bakx et al. 2023; Fujimoto et al. 2022a; Yoon et al. 2022), although robust spectroscopic confirmation of these sources is inevitably required.

In this paper, we present JWST/NIRSpec results of follow-up observations of $z \gtrsim 8.5$ galaxy candidates identified in the first epoch of the Cosmic Evolution Early Release Science (CEERS) Survey. This is the first homogeneous, luminosity-selected follow-up spectroscopy for JWST high-redshift galaxy candidates at $z \gtrsim 8.5$ in the UV luminosity range of $M_{\rm UV} \in [-21, -18]$. This sets the benchmark for the spectroscopic confirmation of large samples of galaxies, further allowing detailed investigations into the UV luminosity function shape at $z \gtrsim 8.5$ and the characterization of the high-redshift Lyman-break galaxy (LBG) population newly identified with JWST. This work is complementary to the recent successful spectroscopic confirmation of the higher redshift, but much (1–2 mag) fainter galaxies at $z = 9.51$–13.20 in lensing cluster fields (Roberts-Borsani et al. 2022; Williams et al. 2023) or very deep observations of the Hubble Ultra Deep Field (Curtis-Lake et al. 2023; Robertson et al. 2023).

The structure of this paper is as follows. In Section 2, we describe the observations and the data reduction of CEERS JWST NIRCam and NIRSpec observations. Section 3 outlines the methods of redshift determination. In Section 4, we present and discuss the results of the validity of the redshift determination and the physical properties for the spectroscopically confirmed sources. A summary of this study is presented in Section 5. Throughout this paper, we assume a flat universe with $\Omega_{\rm m} = 0.3$, $\Omega_\Lambda = 0.7$, and $H_0 = 70$ km s^{-1} Mpc^{-1} and the Chabrier (2003) IMF. We adopt vacuum rest-frame wavelengths for the emission lines. When we show lensed galaxies taken from the literature for comparison, we show the intrinsic properties after magnification corrections.

2. Observations and Data Processing

The JWST/NIRCam (Rieke et al. 2003, 2005; Beichman et al. 2012) and JWST/NIRSpec (Jakobsen et al. 2022) data employed in this work were taken as part of the Cosmic Evolution Early Release Science Survey (CEERS; ERS 1345, PI: S. Finkelstein) in the CANDELS (Grogin et al. 2011; Koekemoer et al. 2011) Extended Groth Strip (EGS) field. The complete details of the CEERS program will be presented in S. Finkelstein et al. (2023, in preparation).

2.1. JWST/NIRCam Data and Target Selection

The galaxies discussed in this work are part of the photometrically selected $z \gtrsim 8.5$ candidate galaxy sample assembled by Finkelstein et al. (2023). These galaxy candidates were selected from the CEERS epoch (1) (2022 June) NIRCam imaging data, which are described in full in Bagley et al. (2023). The Finkelstein et al. (2023) photometry catalog includes measurements over the full NIRCam wavelength range in the F115W, F150W, F200W, F277W, F356W, F410M, and F444W filters, which have exposures of ∼3000

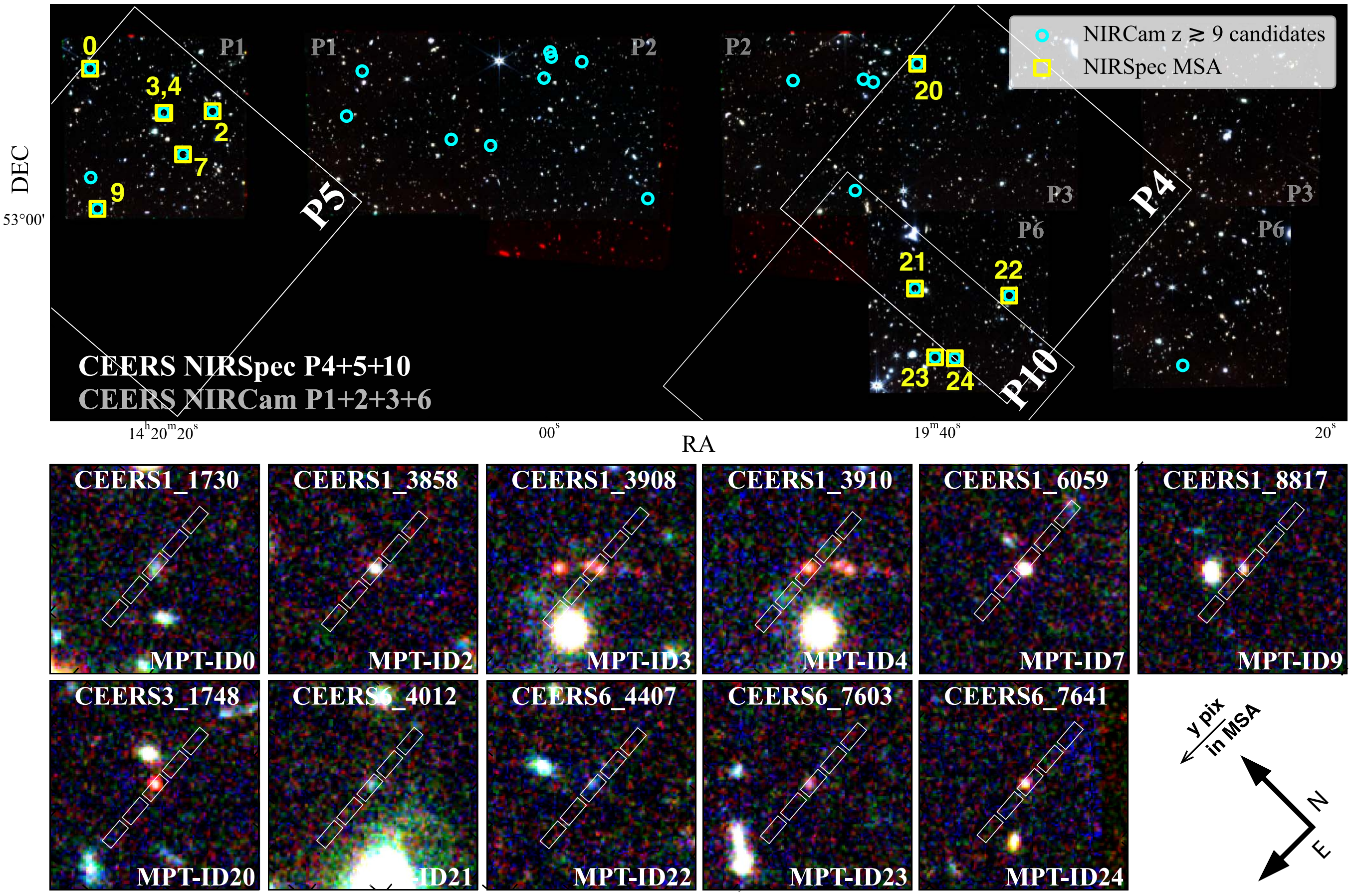

Figure 1. Top: NIRCam red giant branch (RGB) color (R: F444W, G: F356W, B: F277W) mosaic combining the NIRCam pointing IDs of ID1, ID2, ID3, and ID6 taken in CEERS epoch1 (2022 June). The white squares show the NIRSpec MSA footprints of the NIRSpec pointing IDs of ID4, ID5, and ID10 taken in CEERS epoch2 (2022 December). The cyan circles denote the NIRCam-selected high-redshift galaxy candidates at $z \gtrsim 8.5$ presented in Finkelstein et al. (2023). The yellow squares represent the NIRSpec MSA targets, and their MPT-IDs are labeled. Two candidates in the MSA footprints did not receive slits due to the constraints of the MSA configuration. Bottom: RGB $3''\!.6 \times 3''\!.6$ image cutouts around the MSA targets (R: F356W, G: F277W, B: F150W). The rectangles show the $0''\!.2 \times 0''\!.46$ shutter configuration. We use the standard three-shutter MSA slitlets and perform a three-point nodding. Thus, five shutter positions are presented, including the nod positions, which is reflected in the 2D spectra in Figure 2.

s per filter (∼6000 s for F115W); as well as in the existing HST/CANDELS Advanced Camera for Surveys (ACS) and WFC3 F606W, F814W, F105W, F125W, F140W, and F160W bands.

Robust candidate $z \gtrsim 8.5$ galaxies were selected based on a combination of detection significance and photometric redshift distribution criteria, designed to select well-measured astrophysical sources with photometric redshifts highly likely to be at $z \gtrsim 8.5$. This full sample consists of 26 candidate galaxies, with the full details available in Finkelstein et al. (2023). The NIRSpec multiobject spectroscopy (MOS) configurations were designed to maximize the number of these candidates observed, resulting in a total of 11 targets at $z \simeq 9$–13. In Figure 1, we present the source positions of the full 26 candidates and the 11 targets included in the NIRSpec observations. The target properties are summarized in Table 1.

2.2. *JWST/NIRSpec Data*

The $z \gtrsim 8.5$ candidates presented in this work are included in the NIRSpec MOS configurations taken with the Micro Shutter Array (MSA; Ferruit et al. 2022) during the CEERS epoch2 observations (2022 December). These NIRSpec observations are split into 6 different MSA pointings, each of them observed with the G140M/F100LP, G235M/F170LP, and G395M/F290LP medium-resolution ($R \approx 1000$; here denoted by "M") gratings plus the prism ($R \approx 30$–300), fully covering the ∼1–5 μm wavelength range. The MSA was configured to use three-shutter slitlets, enabling a three-point nodding pattern, shifting the pointing by a shutter length in each direction for background subtraction. The total exposure time per disperser is 3107 s distributed as three integrations (one per nod) of 14 groups each in the NRSIRS2 readout mode. Two prism observations (NIRSpec pointings 9 and 10) were affected by an electrical short,[31] and we do not include those data in our analyses in this paper. Those two prism observations were rescheduled in CEERS epoch3 (2023 February), for which the data processing, analyses, and results are presented in Arrabal Haro et al. (2023a).

The M grating and prism observations have different MSA configurations, and so not all targets are observed in both modes. We present spectra of 11 candidates at $z \gtrsim 8.5$ in this study: 7 were observed with the prism, 5 were observed with the M gratings, and two were observed with both modes (see Table 1).

---

[31] Webb Observing Problem Report (WOPR) ID: 88650.

Table 1
NIRSpec Follow-up High-z Targets Identified with NIRCam in CEERS Epoch1

Source ID[a] (1)	MPT-ID (2)	R.A. (deg) (3)	Decl. (deg) (4)	m_{F277W} (mag) (5)	z_{phot} (6)	z_{spec} (7)	S/N (8)	Mode (9)	Other References (10)
Confirmed									
CEERS1_3858	2	214.994402	52.989379	27.2	$8.95^{+0.15}_{-0.18}$	8.807 ± 0.003	7.5	P	1, 2, 3
CEERS1_3908	3	215.005189	52.996580	27.3	$9.04^{+1.29}_{-0.06}$	8.005 ± 0.001[b]	17.5	P	2
CEERS1_3910	4	215.005365	52.996697	28.0	$9.55^{+1.05}_{-0.39}$	7.9932 ± 0.0006	9.6	M	1, 2, 4
CEERS1_6059	7	215.011706	52.988303	27.0	$9.01^{+0.06}_{-0.06}$	8.876 ± 0.002	8.9	P,M	2, 4
CEERS3_1748	20	214.830685	52.887771	28.5	$8.77^{+0.45}_{-1.08}$	7.769 ± 0.003	7.7	P,M	2, 3
CEERS6_7603	23	214.901252	52.846997	28.9	$11.32^{+0.30}_{-1.74}$	8.8805 ± 0.0005[b]	9.8	M	2
CEERS6_7641	24	214.897232	52.843854	28.1	$8.95^{+1.95}_{-0.15}$	8.9980 ± 0.0005[b]	11.1	M	1, 2, 4
Not confirmed									
CEERS1_1730	0	215.010022	53.013641	27.7	$13.36^{+0.84}_{-1.08}$	⋯	⋯	P	
CEERS6_4012	21	214.888127	52.858987	27.6	$8.89^{+0.36}_{-0.36}$	⋯	⋯	M	2
CEERS6_4407	22	214.869661	52.843646	29.0	$10.63^{+0.81}_{-0.57}$	⋯	⋯	M	
Tentative									
CEERS1_8817	9	215.043999	52.994302	28.1	$10.60^{+0.42}_{-0.36}$	9.388? or 9.696?	5.7	P	2

Notes. (1) Source ID used in Finkelstein et al. (2023). (2) Source ID in the NIRSpec MSA configurations. (3) Right ascension (J2000). (4) decl. (J2000). (5) Observed AB total magnitude in the F277W filter. (6) Photometric redshift. (7) Spectroscopic redshift measured from NIRSpec spectroscopy. (8) S/N from the Gaussian +continuum fit for the [O III]5008, 4960 lines. For MPT-ID9, we show the single-line S/N integrated over the 3 pixels around the peak. (9) NIRSpec observation mode (prism (P); medium-resolution gratings (M)). (10) References that also report the source identification as high-redshift ($z \gtrsim 8.5$) galaxy candidates (Bouwens et al. 2023a (1); Donnan et al. 2023a (2); Whitler et al. 2023 (3); Labbe et al. 2023 (4)). (3)–(6) Also taken from Finkelstein et al. (2023).

[a] These three galaxies have also been reported in Tang et al. (2023).

[b] From top to bottom, these sources are referred to as CEERS_4702, 4774, 4777, 7078, 23084, 61381, 61419, 2067, 56878, 57400, and 10332 in Arrabal Haro et al. (2023a).

2.3. NIRSpec Data Reduction

The details of the CEERS NIRSpec data processing will be presented in P. Arrabal Haro et al. (2023, in preparation). We summarize the main steps of the reduction here. The NIRSpec data is processed with the STScI Calibration Pipeline[32] version 1.8.5 and the Calibration Reference Data System mapping 1027. We make use of the `calwebb_detector1` pipeline module to subtract the bias and the dark current, correct the $1/f$ noise, and generate count-rate maps (CRMs) from the uncalibrated images. At this stage, the parameters of the `jump` step are modified for an improved correction of the "snowball" events[33] associated with high-energy cosmic rays.

The resulting CRMs are then processed with the `calwebb_spec2` pipeline module, which creates 2D cutouts of the slitlets, performs the background subtraction making use of the three-nod pattern, corrects the flat-fields, implements the wavelength and photometric calibrations, and resamples the 2D spectra to correct the distortion of the spectral trace. The `pathloss` step accounting for the slit-loss correction is turned off at this stage of the reduction process. Instead, when required for the analysis, we introduce slit-loss corrections based on the morphology of the sources in the NIRCam bands and the location of the slitlet hosting them.

The images of the three nods are combined at the `calwebb_spec3` pipeline stage, making use of customized apertures for the extraction of the 1D spectrum. The custom extraction apertures are visually defined for targets presenting high signal-to-noise ratio (S/N) at the continuum or emission lines, which are easily recognizable in the 2D spectra. For those cases where the targets are too faint for a robust visual identification, a 4 pixel extraction aperture is defined around a spatial location estimated from the relative position of the target within its shutter, derived from the MSA configuration.

Finally, the 2D and 1D spectra are simultaneously inspected with the Mosviz visualization tool[34] (Developers et al. 2023) to mask possible remaining hot pixels and other artifacts in the images, as well as the detector gap (when present). Once inspected and masked, the three M gratings are combined into a single spectrum, resampling to a common wavelength array at the overlapping wavelengths and adopting the mean flux at each pixel, weighted by the flux errors. No resampling of the wavelength grid is performed in the prism spectra.

We test the accuracy of the error spectrum by comparing the normalized median absolute deviation of the science spectrum (masking out emission lines) to the median of the error spectrum. We find that the actual data show fluctuations ∼1.5–2× larger than the typical error value. Thus, we scale the error spectrum up by this scale factor on an object-by-object basis. Our noise correction factor from the above method is consistent with the estimates presented in Arrabal Haro et al. (2023a). Although the effect of noise correlation might still increase the correction factor, any potential impact would likely be modest (∼30%; Arrabal Haro et al. 2023a).

---

[32] https://jwst-pipeline.readthedocs.io/en/latest/index.html

[33] https://jwst-docs.stsci.edu/data-artifacts-and-features/snowballs-and-shower-artifacts

[34] https://jdaviz.readthedocs.io/en/latest/mosviz/index.html

3. Analysis

3.1. Line Identification

We systematically analyze the reduced 1D and 2D spectra of the 11 spectroscopically observed targets to identify emission line and continuum features. From 7 targets (MSA Planning Tool (MPT)-ID2, ID3, ID4, ID7, ID20, ID23, and ID24), we identify at least two emission line features whose wavelength separations and flux ratios match those of the [O III]5008, 4960 emission lines. These line features have $S/N \gtrsim 7$ and $S/N \gtrsim 3$ from the brighter and the fainter doublet line, respectively, based on the integrated pixel S/N over 3 pixels around the peak. In Figure 2, we show the 1D and 2D spectra of these seven targets.

From one additional target (MPT-ID9), a single-line feature is observed with S/N >5 at 5.20 μm, suggesting a potential identification of [O III]5008 at $z = 9.388$, or Hβ at $z = 9.696$. However, no positive signals at the expected wavelengths for the neighboring lines are confirmed in those potential redshift solutions with Hβ, [O III]5008, or [O III]4960. This suggests that the neighboring lines are buried in the noise fluctuations or that the 5.20 μm line feature is just noise. We thus focus on the first seven sources with at least two significant line features in the following analyses. From the other three targets (MPT-ID0, ID21, ID22), we identify no secure line or Lyα break features. Interestingly, three out of these four potential and nondetected sources are estimated to have $z_{\rm phot} > 10$ (Finkelstein et al. 2023), suggesting that these sources might be truly located at $z > 10$, where the typical strong rest-frame optical emission lines (Hβ, [O III]5008, 4960) would lie beyond the red limit of NIRSpec wavelength coverage, making the redshift estimate challenging. The 1D and 2D spectra for these four targets are shown in the Appendix.

3.2. Redshift Measurement

For the seven sources with at least two possible line features, first, we perform template fitting to the NIRSpec 1D spectra to obtain initial redshift estimates. A linear combination of three different CIGALE (Burgarella et al. 2005; Noll et al. 2009; Boquien et al. 2019) models is fitted to the real spectra at a redshift interval, with steps matching the spectral resolution of the grating (or the highest spectral resolution at the red wavelengths in the case of the prism). The templates employed are selected to represent a wide range of galaxy spectra, from emission line galaxies to quiescent and old massive galaxies. For all the sources spectroscopically confirmed, the best solution from χ^2 minimization over the explored $z = 0$–13 range is consistent with an [O III]5008 detection at long wavelengths.

Using the best-matching template redshifts as the starting estimation, we perform a Gaussian + continuum fitting with a Markov Chain Monte Carlo (MCMC) approach around the peak of the brightest emission line to refine the redshift measurements. Because these prior redshift estimates suggest that the brightest emission line corresponds to [O III]5008 in all seven sources, we adopt the vacuum rest-frame wavelengths of 5008.22 Å and 4960.28 Å for the fit to the brightest and neighboring lines simultaneously by assuming that their line widths and the underlying continuum are the same and the line ratio of 3:1. We determine spectroscopic redshifts in the range $z_{\rm spec} = 7.7621$–8.9979. We summarize our final $z_{\rm spec}$ measurements and 1σ uncertainties in Table 1. In the right panel of Figure 2, the red line and blue curve show our $z_{\rm spec}$ value compared to the photometric redshift probability distribution $P(z)$ presented in Finkelstein et al. (2023) based on the photometric spectral energy distribution (SED) analysis, respectively. We confirm that the $z_{\rm spec}$ values of all these seven sources are consistent with the $P(z)$ distribution within 2σ. We further discuss the difference between $z_{\rm spec}$ and $z_{\rm phot}$ in Section 4.1. We detect the Lyα continuum break only from the prism spectrum of MPT-ID7, where we confirm the wavelength of the continuum break is consistent with the redshift determined by the emission lines. We show the Lyα break observed in MPT-ID7 in the Appendix.

Note that MPT-ID3 and ID4 are separated by less than 3 kpc in physical scale (see Figure 1), and our $z_{\rm spec}$ measurements are $z = 8.005 \pm 0.001$ for ID3, and $z = 7.9932 \pm 0.0006$ for ID4. Although the line feature is less evident in ID4, these independent results suggest that ID3 and ID4 are a close pair, and our $z_{\rm spec}$ estimate for ID4 is secure. We also note that the [O III]5008 line feature in the 2D spectrum of MPT-ID2 is less clear than those for other sources. However, we confirm that the S/N increases to 7.5 in the simultaneous fit to both [O III] lines by fixing the wavelength separation and the line ratio. The $z_{\rm spec}$ value also shows an excellent agreement with $z_{\rm phot}$. We thus include MPT-ID2 in our $z_{\rm spec}$ sample in this paper.

We also run the template fitting for the remaining four sources in order not to miss the chance that we identify multiple marginal line detections whose wavelength separation matches with a specific redshift solution. However, we do not find any convincing redshift solutions for these sources.

3.3. Line Flux Measurement

We evaluate the fluxes of several key rest-optical emission lines for the $z_{\rm spec}$ sample. We focus on the line fluxes of [O III]5008, [O III]4960, Hβ, and [O II]3728 in this paper. We perform the Gaussian + continuum profile fitting by fixing the redshift. We fit [O III]5008, [O III]4960, and Hβ lines simultaneously, while we separately fit [O III]3727. In the fitting, we assume the same line width in the velocity frame among these emission lines. We also assume that the same underlying continuum among the [O III]5008, [O III]4960, and Hβ lines and fix the line ratio of 3:1 between [O III]5008 and [O III]4960. We use the rest-frame 4100–5200 Å for the fit to obtain a stable result for the underlying continuum. For MPT-ID24 the wavelength of the Hβ line falls in the detector gap, while the Hγ line is detected at $S/N \sim 3$. We thus alternatively evaluate the line flux of Hγ and convert it to Hβ with Hγ/Hβ of 0.471 for the case B recombination with the electron temperature of 10^4 K without dust correction (Osterbrock 1989) due to the negligible dust extinction estimated from our SED analysis (Section 3.5).

In Table 2, we list the rest-frame equivalent width (EW) values of [O III]5008 and Hβ and R3 ($\equiv$[O III]5008/Hβ). When we do not securely constrain the Hβ flux at more than $S/N = 2$, we place 3σ upper and lower limits for EW(Hβ) and R3, respectively. When the continuum is not well constrained ($S/N < 2$) from the fit, we estimate the underlying continuum by correcting the slit-loss for the line emission (see Section 3.4) and subtracting the line contribution to the F444W photometry. We confirm that our EW measurements are consistent with the independent analysis and measurement for MPT-ID3,ID 23, and ID24 presented in Tang et al. (2023) within the errors.

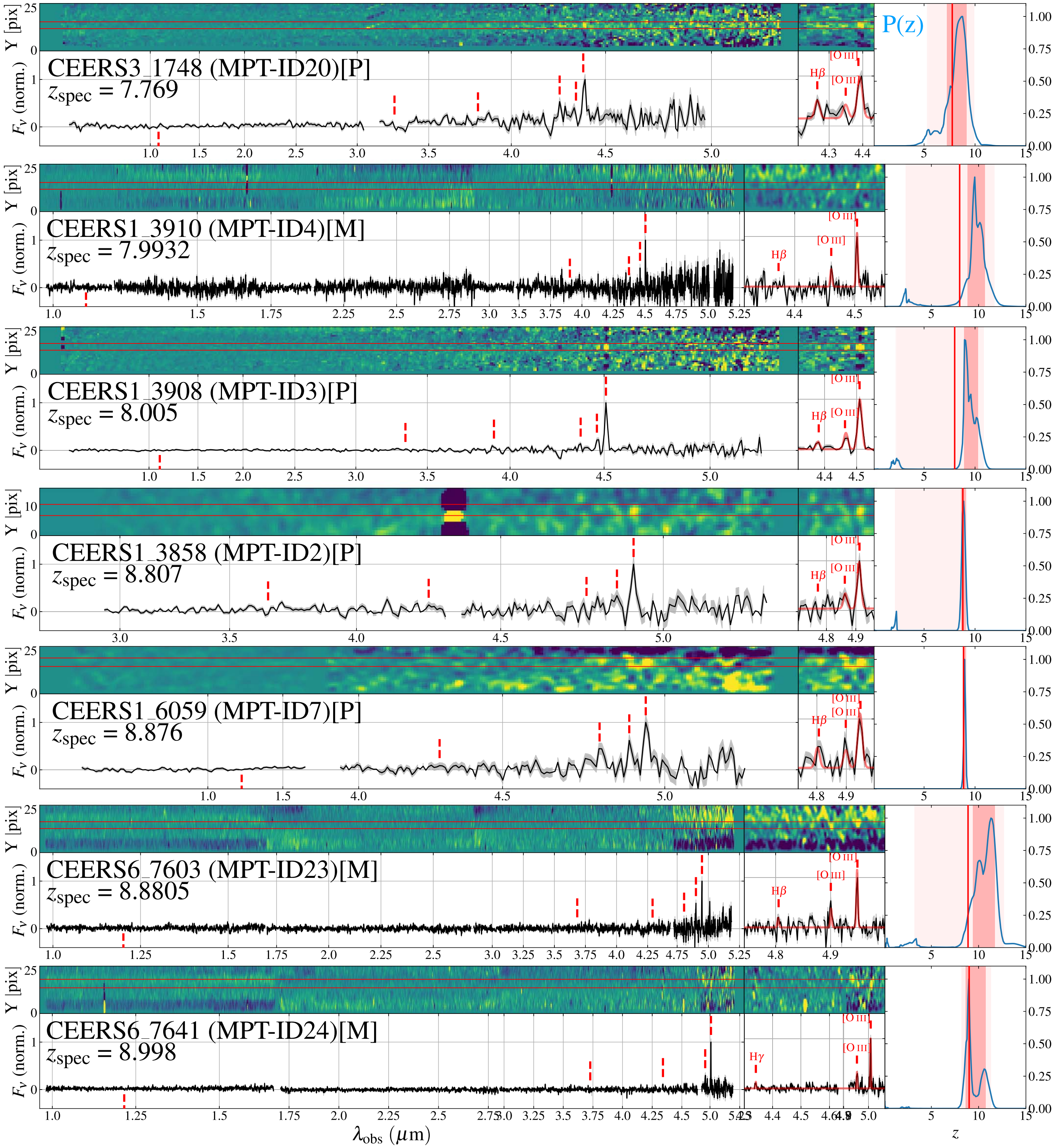

Figure 2. NIRSpec 2D (top) and 1D (bottom) spectra in the observed wavelength frame for the sources that are spectroscopically confirmed. MPT-ID20, ID3, ID2, and ID7 show the prism spectrum, while ID4, ID23, and ID24 show the combined spectra of the G140M, G235M, and G395M gratings. The red horizontal lines on the 2D spectrum represent the aperture position used for extracting the 1D spectrum. The red vertical dashed lines denote the expected wavelengths of Lyα, [O II] 3727, Hγ, Hβ, [O III]4960, and [O III]5008 from left to right based on our $z_{\rm spec}$ measurement. The 2D spectrum is smoothed with a one-pixel (=σ) Gaussian kernel. The middle panel shows the zoom-in spectrum around the brightest line feature. The best-fit Gaussian + continuum fit is overlaid on the 1D spectrum. The right panel presents the photometric redshift probability distribution $P(z)$ as the blue curve, while the red vertical line represents the $z_{\rm spec}$ value. The dark and light red shaded regions indicate 68% and 95% confidence intervals of $P(z)$, respectively, from the photometric redshift analysis (Finkelstein et al. 2023). For sources observed in both the prism and medium grating modes, we show here the spectrum with the better S/N in the brightest emission line.

We do not detect [O II] with $S/N > 2$ from any of the $z_{\rm spec}$ sources. We thus place 3σ upper limits on the [O II] line and list the 3σ lower limits of O32 (≡[O III]5008/[O II]3727) in Table 2. We do not apply the slit-loss corrections for this calculation. Due to the wavelength dependence of the JWST point-spread function, the slit-losses should be smaller for

Table 2
Physical Properties of the NIRCam CEERS Galaxies Confirmed at $z \simeq 8 - 9$

MPT-ID (1)	$z_{\rm spec}$ (2)	$M_{\rm UV}$ (mag) (3)	$E(B-V)$ (mag) (4)	SFR ($M_\odot$ yr^{-1}) (5)	$M_{\rm star}$ ($10^8 M_\odot$) (6)	$f_{\rm burst}$ (7)	EW([O III]5008) (Å) (8)	EW(Hβ) (Å) (9)	R3 (10)	O32 (11)	Mode (12)
2	8.807	−20.44	$0.03^{+0.03}_{-0.02}$	$3.2^{+1.1}_{-0.5}$	$1.2^{+0.8}_{-0.6}$	$0.12^{+0.18}_{-0.08}$	372 ± 112	<150	>2.5	>8.2	P
3	8.005	−20.47	$0.15^{+0.04}_{-0.07}$	$9.8^{+2.9}_{-3.2}$	$2.0^{+1.7}_{-0.8}$	$0.25^{+0.21}_{-0.16}$	1022 ± 129	163 ± 62	6.3 ± 2.3	>8.1	P
4	7.9932	−19.44	$0.33^{+0.12}_{-0.09}$	$16.3^{+21.0}_{-8.1}$	$8.7^{+6.3}_{-4.4}$	$0.10^{+0.18}_{-0.07}$	430 ± 69	<166	>2.6	…[a]	M
7	8.876	−20.75	$0.03^{+0.03}_{-0.02}$	$3.9^{+1.1}_{-0.6}$	$1.2^{+0.9}_{-0.6}$	$0.13^{+0.25}_{-0.09}$	895 ± 436	350 ± 194	2.6 ± 0.8	>5.5	M
20	7.769	−18.55	$0.61^{+0.02}_{-0.18}$	$64.3^{+18.6}_{-50.8}$	$30.6^{+19.7}_{-13.0}$	$0.08^{+0.13}_{-0.06}$	109 ± 19	50 ± 16	2.2 ± 0.8	>6.1	P
23	8.8805	−18.38	$0.06^{+0.1}_{-0.04}$	$0.8^{+0.7}_{-0.3}$	$0.2^{+0.2}_{-0.1}$	$0.21^{+0.23}_{-0.14}$	1195 ± 200	208 ± 121	5.8 ± 3.3	>6.5	M
24	8.998	−19.08	$0.09^{+0.08}_{-0.06}$	$2.7^{+1.5}_{-1.0}$	$0.6^{+0.6}_{-0.3}$	$0.23^{+0.22}_{-0.15}$	989 ± 131	173 ± 51[b]	5.7 ± 1.7	>5.0	M

Notes. (1) Source ID. (2) Spectroscopic redshift. (3) Absolute UV luminosity, calculated from the F150W filter. (4) Dust extinction. (5) Average SFR over 10 Myr. (6) Stellar mass. (7) Fraction of the stellar mass produced by the young (<10 Myr) stellar population. (8) Rest-frame equivalent width of [O III]5008 line. (9) Rest-frame equivalent width of Hβ line. (10) [O III]5008/Hβ ratio. (11) [O III]5008/[O II]3727 ratio. (12) NIRSpec observation mode (prism (P); medium resolution (M)). For the sources observed in both modes, we adopt the results with the better S/N in the brightest emission line. (4)–(7) Values are estimated from the SED analysis with CIGALE, while (8)–(11) values are derived from the NIRSpec observations.

[a] The [O II] line wavelength falls in the detector gap.

[b] The Hβ line wavelength falls in the detector gap, while we evaluate the Hβ flux from the Hγ detection (see text).

[O II] compared to those for [O III], and a slit-loss correction would increase O32. Thus, the uncorrected lower limit for O32 is a conservative estimate.

Note that there are several other line features that show peak pixel values with S/N ∼ 1–3 at the expected wavelength positions (e.g., [Ne III], N V) in the 1D spectra, while in most of the cases, the y-axis position of the positive signals within the extracted aperture is not exactly matched with that of the brightest [O III]5008 line. Although we cannot rule out the possibility of different spatial distributions for different emission lines[35] or the effect of noise fluctuations in these low S/N spectra, we do not focus on the other emission lines in this paper.

We also note that several spectra exhibit negative and weak positive traces distinct from the target positions (e.g., MPT-ID7 and ID23). We do not find any excessively bright background values that would indicate unknown open shutters in one or more nods. However, we observe small background variations in some observations among different nods, which likely cause the negative and positive traces due to over-subtraction and/or under-subtraction of the background. We further confirm that the relative positions of the negative and positive traces are consistent with cases where the background becomes relatively high in one nod. The background subtraction and integration process using the standard three-nod approach in the NIRSpec MSA observations[36] ensures that variations in the background do not impact the shutters containing the target, and thus our flux estimate remains unaffected by this effect.

3.4. Slitloss Correction

As mentioned in Section 2.3, we do not apply the default slitloss correction implemented in the calibration pipeline. Instead, we evaluate the scaling factor for the slit-loss correction in the two following approaches. In the first approach, we convolve and integrate the 1D spectrum with the NIRCam F444W filter response function. By comparing the resulting value with the actual total galaxy flux measured with the NIRCam F444W filter, we can assess the flux loss in the 1D spectrum and derive a scaling factor. In the second approach, we calculate the flux in the F444W image enclosed within the $0\farcs2 \times 0\farcs46$ shutter based on the source and MSA shutter positions and estimate the scaling factor to match it with the total flux measurement. We find that MPT-ID4 and ID7 show negative scaling factors in the first approach, indicating that the integrated F444W spectral fluxes are dominated by noise fluctuation, even with the inclusion of the strong line emission in these sources. We thus adopt the second approach for MPT-ID4 and ID7, while we use the first for the rest of our targets. When we compare these two approaches using some bright targets, we find that the scaling factor can be different by ∼10%–40%. This may be due to unknown offsets of targets within the MSA shutter related to the accuracy of the MSA alignment or may indicate uncertain relative photometric calibration between NIRCam and NIRSpec, which cannot be corrected in the second approach. Diffraction losses within NIRSpec (Jakobsen et al. 2022), which are not included in the second approach, could also be a possible reason for the difference. An extended [O III]+Hβ structure has been identified around a lensed galaxy at $z = 8.5$ (Fujimoto et al. 2022b), and the differential spatial distribution between the ionized gas and the underlying continuum emission is also another unknown uncertainty in both approaches. We thus caution the readers that additional uncertainty might exist in the measurements due to the slit-loss correction steps.

3.5. SED Analysis

We analyze the physical properties of the seven spectroscopically confirmed NIRCam galaxies using CIGALE. The details will be presented in D. Burgarella et al. (2023, in preparation), and here we briefly explain our SED model. We include the HST+JWST/NIRCam photometry as well as the EW([O III]5008) in the fit. We use the stellar synthesis population model of BPASS-v2 (Eldridge et al. 2017) with the lowest available Z_BPASS = 0.0001, where $Z_\odot = 0.014$. We assume a delayed + final exponential burst (younger than 10 Myr) star formation history (SFH): SFR(t) $\propto t/\tau_0^2 \times \exp(-t/\tau_0) + k \times \exp(-t/\tau_1)$ with the mass fraction from the

---

[35] For example, spatial offsets between the faint AGNs and the hosts have been reported in Ding et al. (2022), where highly ionized emission lines might be observed with spatial offsets.

[36] https://jwst-docs.stsci.edu/jwst-near-infrared-spectrograph/nirspec-operations/nirspec-dithers-and-nods/nirspec-mos-dither-and-nod-patterns

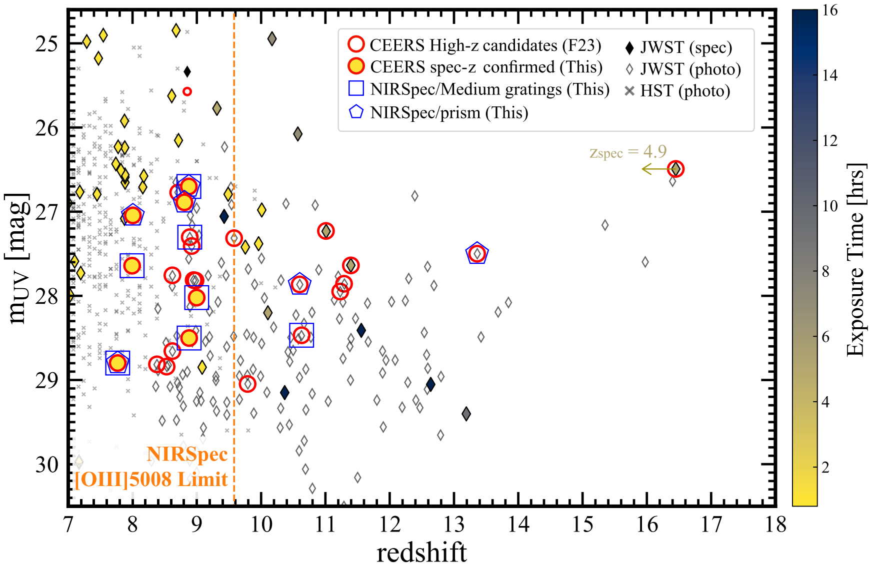

Figure 3. Status of spectroscopic confirmation at $z \gtrsim 8$ with JWST. The vertical axis represents the apparent UV magnitude. The red open circles show the 26 candidates at $z \gtrsim 8.5$ in CEERS presented in Finkelstein et al. (2023), and the filled circles indicate the sources spectroscopically confirmed in this study. The open blue pentagons and squares indicate the observation mode of prism and medium gratings, respectively. Among the 26 candidates, the highest-redshift candidate at $z_{\rm phot} \sim 17$ is spectroscopically determined to have $z = 4.9$, while two other candidates are confirmed at $z = 11.4$, and $z = 11.0$ (Arrabal Haro et al. 2023b; Harikane et al. 2023a). The color diamonds indicate other $z_{\rm spec}$ confirmed galaxies taken from recent JWST studies from lensing cluster fields (Roberts-Borsani et al. 2022; Wang et al. 2022; Williams et al. 2023; Mascia et al. 2023) and general fields (Curtis-Lake et al. 2023; Arrabal Haro et al. 2023a, 2023b; Bunker et al. 2023; Harikane et al. 2023a; Tang et al. 2023). No magnification corrections are applied to the lensed sources. The color of the circles and diamonds corresponds to the exposure time of the JWST/NIRSpec denoted in the color bar. The gray crosses and open diamonds present photometric high-z candidates from the literature identified with HST and JWST, respectively. The dashed vertical line presents the redshift limitation to detect the [O III]5008 line with NIRSpec, indicating the potential challenges of the $z_{\rm spec}$ determination beyond $z \sim 9.6$ with a short exposure for faint objects due to the lack of bright emission lines.

recent burst activity of $f_{\rm burst} = 0.0 - 0.5$. We adopt the dust attenuation law from Calzetti et al. (2000) for the stellar continuum and a screen model with an SMC extinction curve (Pei 1992) for the nebular emission (continuum + lines). During the SED fitting, we assume the $E(B-V)_{\rm stellar} = 0.5 \times E(B-V)_{\rm line}$. Interested readers are referred to Boquien et al. (2019) for specific modeling procedures using CIGALE. The results for the SFR, $M_{\rm star}$, $E(B-V)$, $f_{\rm burst}$ are summarized in Table 2. From the median values, our NIRCam-selected spec-z confirmed sources are generally characterized as SFR $\simeq 4\,M_\odot$ yr^{-1}, $M_{\rm star} \simeq 10^8\,M_\odot$ yr^{-1}, $E(B-V) \simeq 0.1$, and $f_{\rm burst} \simeq 10\%$. Note that the SED analysis with the spatially integrated photometry may systematically underestimate the stellar mass, especially in the strong emission line systems (Giménez-Arteaga et al. 2023; Papovich et al. 2022). In our analysis, this effect is mitigated by constraining the $f_{\rm burst}$ factor to the range 0%–50%, which provides the median of $f_{\rm burst} \simeq 20\%$ in our sample. The $f_{\rm burst} \simeq 10\%$ is consistent with recent results of the pixel-based spatially resolved SED analysis for lensed galaxies at $z = 5 - 8.5$ with NIRCam (Giménez-Arteaga et al. 2023). The consistency and potential differences among different SED models are further discussed in D. Burgarella et al. (2023, in preparation).

4. Results and Discussions

4.1. Validity of High-redshift Galaxy Selection

In Figure 3, we present the distribution of UV apparent magnitudes ($m_{\rm UV}$) versus redshift (spectroscopic where available; otherwise photometric) for NIRCam-selected galaxies from CEERS (Finkelstein et al. 2023) and other recent JWST photometric (Bouwens et al. 2021, 2023a, 2023b; Adams et al. 2023; Atek et al. 2023; Bradley et al. 2022; Castellano et al. 2022; Morishita & Stiavelli 2023; Naidu et al. 2022b; Donnan et al. 2023a, 2023b; Harikane et al. 2023b; Pérez-González et al. 2023) and spectroscopic studies (Curtis-Lake et al. 2023; Roberts-Borsani et al. 2022; Wang et al. 2022; Williams et al. 2023; Arrabal Haro et al. 2023a, 2023b; Bunker et al. 2023; Harikane et al. 2023b; Mascia et al. 2023; Tang et al. 2023). When necessary, we convert the absolute UV magnitudes reported in the literature to the apparent magnitudes based on their $z_{\rm spec}$ or $z_{\rm phot}$ values. For the $z_{\rm spec}$ sources, the color of the symbols corresponds to the exposure time of the follow-up NIRSpec observations. No magnification correction is applied to the lensed sources.

Among our 11 NIRCam-selected high-redshift galaxy candidates, we confirm the spectroscopic redshifts of 7 galaxies at $z = 7.769 - 8.998$. Our CEERS observations demonstrate the capability of NIRSpec to determine the redshift even with a ∼50 min exposure down to $m_{\rm UV} \simeq 29$ mag at $z \simeq 9$ ($M_{\rm UV} \simeq -18$ mag). On the other hand, our results suggest that the $z_{\rm spec}$ confirmation at $z \gtrsim 10$ is still challenging due to the lack of strong emission lines observable at these higher redshifts within the NIRSpec wavelength coverage. The successful cases at $z \gtrsim 10$ in the literature are achieved mainly by the identification of the Lyα break (e.g., Curtis-Lake et al. 2023; Arrabal Haro et al. 2023a, 2023b), which is likely owing to deep exposures (>5 hr) and/or the brightness of the target ($m_{\rm UV} < 27.5$ mag) even with the similarly short exposure (∼1 hr). The slitloss may also affect the success ratio of the $z_{\rm spec}$ determination for a given source flux.

If we examine the success ratio based on each redshift range according to the original $z_{\rm phot}$ estimates of our targets, we achieve the spectroscopic confirmation in six out of seven (≃90%) targets with $8.8 \lesssim z_{\rm phot} \lesssim 9.5$. Owing to the homogeneous sample selection and sensitivity in the follow-up

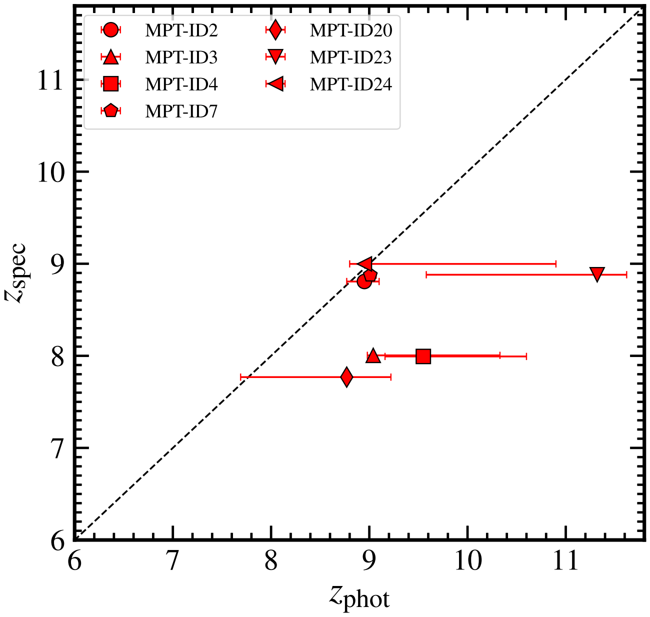

Figure 4. Photometric vs. spectroscopic redshift for the NIRCam-selected galaxies with $z_{\rm phot} \gtrsim 8.5$. Six out of seven sources show $z_{\rm spec} < z_{\rm phot}$; though, all are consistent within 2σ.

spectroscopy, our results indicate that the classical $z_{\rm phot}$ technique assures at least ~90% of the high-redshift galaxy selection at $z \simeq 9$. This is helpful to interpret the recent and future UVLF results out to $z \simeq 9$ that are also measured via similar dropout or $z_{\rm phot}$ techniques with NIRCam (e.g., Bouwens et al. 2023a, 2023b; Donnan et al. 2023a; Harikane et al. 2023b). Importantly, CEERS does not include an NIRCam-based dropout filter for the $z \simeq 9$ galaxy selection (e.g., F090W), and instead, it relies on the HST/ACS F814W filter with a 5σ limiting AB magnitude for a point source of 28.3 mag (Finkelstein et al. 2023). Therefore, a reliable high-redshift galaxy selection could be further improved by the addition of a deeper NIRCam dropout filter.[37]

Interestingly, the majority of our $z_{\rm spec}$ sample has a $z_{\rm spec}$ value smaller than the $P(z)$ peak. In Figure 4, we compare the $z_{\rm phot}$ and $z_{\rm spec}$ values for our $z_{\rm spec}$ sample. Although all $z_{\rm spec}$ values fall within the 95% confidence range of $P(z)$ (see Figure 2), three out of seven sources show $z_{\rm spec} < z_{\rm phot}$ beyond the 68% confidence interval. The $z_{\rm phot}$ value and the entire $P(z)$ shape largely depend on the galaxy models used in the SED fitting. In our original target selection (Section 2.1), the high-redshift galaxy candidates are selected by using the SED fitting code EAZY (Brammer et al. 2008) based on the FSPS-based (Conroy & Gunn 2010) default 12 template sets in EAZY and 6 additional templates presented in Larson et al. (2022). These six additional templates are created by combining stellar population spectra from BPASS (Eldridge & Stanway 2009) and CLOUDY (Ferland et al. 2017) to recover the rest-frame UV blue color space of young galaxies, which significantly recovers the color space of simulated early galaxies in a semianalytic galaxy model (Yung et al. 2022). However, the high fraction of $z_{\rm spec} < z_{\rm phot}$ observed in our sample might indicate that the SED templates generally used in the high-redshift galaxy studies are still insufficient to recover the rest-frame UV color space of $z \gtrsim 8.5$ galaxies, or that the modeling of the IGM is incomplete in some way (though likely *not* due to the damping wing effect discussed in Curtis-Lake et al. 2023, which would lead to redshift differences much smaller than we observe here). This could also show the possible limitations inherent in using a single photo-z code (e.g., Dahlen et al. 2013). Another reason might be the difficulty of determining the redshift at $z \gtrsim 9.5$ due to the lack of strong emission lines in the NIRSpec wavelength coverage. Then, while the true redshifts are distributed on both sides of the peak of $P(z)$ according to uncertainties in the broadband photometry, the spec-z confirmation may be biased to $z \lesssim 9.5$ when the sensitivity is not deep enough to capture the Lyα break (Curtis-Lake et al. 2023; Roberts-Borsani et al. 2022; Robertson et al. 2023) and has to rely on the line identification to determine $z_{\rm spec}$. The absence of the NIRCam-based dropout filter may also at least partially contribute to the $>1\sigma$ difference between $z_{\rm phot}$ and $z_{\rm spec}$ for these sources. For further discussion on this topic, readers are referred to Arrabal Haro et al. (2023a; see Section 4.2).

Of the other four targets with $z_{\rm phot} > 10$, one target turns out to have $z_{\rm spec} = 8.8802$ (MPT-ID23), while no robust lines are identified in the other three targets. The lack of lines might be because [O III]+Hβ is redshifted beyond the NIRSpec wavelength range at $z \gtrsim 10$. Given that one out of four has been confirmed at $z_{\rm spec} < 10$, this would imply that 75% (=3/4) candidates might be truly at $z > 10$, although we cannot rule out the alternative possibility that the remaining three candidates have entirely incorrect redshifts at $z \ll 10$, and their emission lines are fainter than the current NIRSpec sensitivity. Once the success rate of the high-redshift galaxy selection is also confirmed at $z_{\rm phot} \gtrsim 10$, again, it will be widely helpful to interpret the photometric-based UVLF measurements, which are now explored out to $z \sim 17$ with NIRCam (e.g., Bouwens et al. 2023a, 2023b; Donnan et al. 2023a, 2023b; Finkelstein et al. 2023; Harikane et al. 2023b). This will enable us to verify the recent arguments of the high abundance of bright galaxies at these early epochs of the universe, which may challenge the current galaxy formation and evolution models.

4.2. Properties of Galaxies at z = 8–9

The high $z_{\rm spec}$ confirmation rate (≃90%) for the $z_{\rm phot} = 8.5 - 9.6$ targets from the homogeneous LBG selection indicates that our spec-z sample is representative of the majority of the NIRCam-selected LBG population at this redshift. Moreover, recent UVLF studies suggest that the characteristic UV luminosity is $M^{\star}_{\rm UV} \sim -21$ mag in the Schechter function form (e.g., Finkelstein et al. 2015; Bouwens et al. 2021b; Harikane et al. 2023b). Therefore, our NIRCam-selected $z_{\rm spec}$ sources, ranging in the UV luminosity range $M_{\rm UV} \in [-21, -18]$, are sub-$L^{\star}$ populations down to $\simeq 0.06 \times L^{\star}$, which is helpful to understand the typical physical properties of the abundant faint population without gravitational lensing uncertainties. In the following subsections, we thus carry out the first census of the physical properties of spectroscopically confirmed sub-$L^{\star}$ galaxies at this redshift range and investigate the potential difference from bright galaxies ($M_{\rm UV} \simeq -22$) identified in previous HST studies and also spectroscopically confirmed at similar redshifts (R. Larson et al. 2023, in preparation).

---

[37] For example, the GLASS-JWST (Treu et al. 2022) survey includes the F090W filter, where robust $z = 11 - 13$ candidates have been reported (e.g., Castellano et al. 2022; Naidu et al. 2022a).

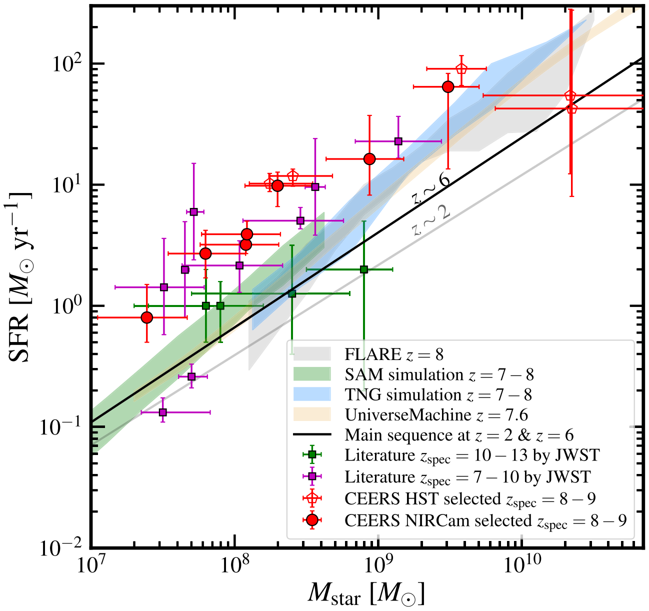

Figure 5. SFR vs. $M_{\rm star}$. The filled and open symbols represent the spec-z and photometric samples, respectively. The filled red circles show our $z_{\rm spec}$ sample. The magenta and green squares are recent JWST results for lensed galaxies at $z\sim7-10$ (Heintz et al. 2022; Roberts-Borsani et al. 2022; Tacchella et al. 2023; Williams et al. 2023) and for general field galaxies at $z\sim10-13$ (Curtis-Lake et al. 2023; Robertson et al. 2023), respectively. The red pentagons show recent HST+IRAC results for bright galaxies at $z\sim8-9$ in the EGS field (Tacchella et al. 2022). The black and gray lines denote the best-fit relations at $z=2$, and $z=6$ (Iyer et al. 2018). The color-shaded regions present the 16th–84th percentile of simulated galaxies (Behroozi et al. 2019, 2020; Yung et al. 2019b, 2022; Wilkins et al. 2023, 2022). Our NIRCam-selected $z_{\rm spec}$ galaxies show high sSFR ($\simeq$40 Gyr^{-1}) compared to the $z=2-6$ main sequence.

4.2.1. *SFR versus* M*star*

Figure 5 presents the SFR–$M_{\rm star}$ relation. For comparison, we show the main sequence estimated at $z=2$, and $z=6$ (Iyer et al. 2018), recent JWST results for the sources spectroscopically confirmed at $z=7-13$ (Curtis-Lake et al. 2023; Heintz et al. 2022; Roberts-Borsani et al. 2022; Robertson et al. 2023; Tacchella et al. 2023; Williams et al. 2023), the HST-selected, brighter LBGs ($M_{\rm UV}\simeq-21.5$) spectroscopically confirmed at $z=8-9$ in CEERS (R. Larson et al. 2023, in preparation), and the 16th–84th percentile of the distribution of simulated galaxies at $z=7-8$ (Behroozi et al. 2019, 2020; Nelson et al. 2019; Yung et al. 2019b, 2022; Wilkins et al. 2023, 2022). Note that we use the SED-based SFR estimate (Section 3.5), instead of using the Hβ line. This is because of the potential uncertainty in the slit-loss correction (Section 3.4). Also, an extended [O III]+Hβ structure has been recently reported around a lensed galaxy at $z=8.5$, which might make the Hβ-based SFR measurement be overestimated by counting the Hβ emission caused by other physical mechanisms such as powerful outflows (Fujimoto et al. 2022b).

In Figure 5, we find that our NIRCam-selected sample (red-filled circles) has a SFR–$M_{\rm star}$ relation generally consistent with the recent JWST results for lensed galaxies at $z=7$–10 (magenta squares) down to $\sim7\times10^7\,M_\odot$. These galaxies from our and recent JWST studies are generally less star-forming and less massive than the HST-selected bright galaxies at similar redshifts (red open pentagons). We also find that most of our $z_{\rm spec}$ sample and the lensed galaxies in the literature fall above the $z=6$ main sequence by $\sim$0.5 dex scale beyond the errors at a given $M_{\rm star}$, showing a relatively high specific SFR (sSFR $\equiv$SFR$/M_{\rm star}$) of $\simeq$40 Gyr^{-1}. In comparison, two out of five CEERS HST-selected galaxies fall close to the $z=6$ main sequence. This finding is in line with recent JWST results that less luminous LBGs at $z\sim7-8$ have similarly high sSFR of $\simeq$80 Gyr^{-1} (Endsley et al. 2023). As discussed in Endsley et al. (2023), the high sSFR in the less luminous LBGs, highlighted by our $z_{\rm spec}$ sample and the lensed galaxies, is likely caused by young stellar populations. This is consistent with our SED results showing the presence of the young stellar populations (<10 Myr) accounting for the total mass of $\simeq$20% of the galaxy mass (Table 2). The increasing sSFR trend as a function of redshift has been observed at lower redshifts (e.g., Tacconi et al. 2013; Speagle et al. 2014; Tasca et al. 2015; Khusanova et al. 2020). Our results may indicate that this increasing trend continues at least out to $z=8-9$, which is predicted from the simulations due to the increased gas accretion rate onto dark matter halos at higher redshifts (e.g., Behroozi et al. 2013). In fact, we also confirm the general agreement with predictions from the simulations within the errors.

Note that a different SFH assumption may impact our SED estimates. For example, our parametric (delayed + final burst <10 Myr) approach might miss an extended tail of older star-forming activity in the SFH. However, we confirm that the mass estimate increases by a factor of $\sim$2 at most in our sample by using the `Dense Basis` (Iyer et al. 2019) fitting code with a nonparametric SFH assumption, which is still insufficient to match the distribution with the main sequence at $z=2-6$. The general agreement with measurements from a variety of literature sources for lensed galaxies also suggests that the impact from different SFH assumptions and SED modelings is likely small. It should also be noted that the slight excess of the observational results compared to the distribution of the simulated galaxies at $z=7-8$ might be caused by the observation bias, which is not counted in the simulated galaxies due to the difficulty of quantifying the spec-z confirmation process in the observation. However, the main sequence at $z=2-6$ is also measured by observations that should include a similar bias. Therefore, the relatively high sSFR of the $z=8-9$ galaxies, compared to that of the $z=2-6$ galaxies, is unlikely explained by the observation bias.

4.2.2. *[O III]+Hβ EW*

In the previous subsections, the sSFR values determined for our $z_{\rm spec}$ sources are higher than those for $z\sim6$ main-sequence galaxies, which is likely because of the young stellar populations at higher redshifts. From a photometric-based SED analysis, high EW([O III]+Hβ) values (>1000 Å) have been inferred for galaxies at $z\simeq$ 6–9 in previous HST+IRAC studies (e.g., Labbé et al. 2013; De Barros et al. 2019; Endsley et al. 2021), where the high EW([O III]+Hβ) is thought to be caused by the light from very young (1–10 Myr) stellar populations (e.g., Amorín et al. 2017; Tang et al. 2019; Vanzella et al. 2020). To have an independent insight into the stellar population and ISM properties of our galaxies, we thus compare the EW([O III]+Hβ) values of our NIRCam-selected galaxies with those of other galaxy populations in this subsection.

In Figure 6, we show the median (red line) and 16th–84th percentile (red bar) of the rest-frame [O III]+Hβ EW measurement for our $z_{\rm spec}$ sample. In the same manner, we also measure

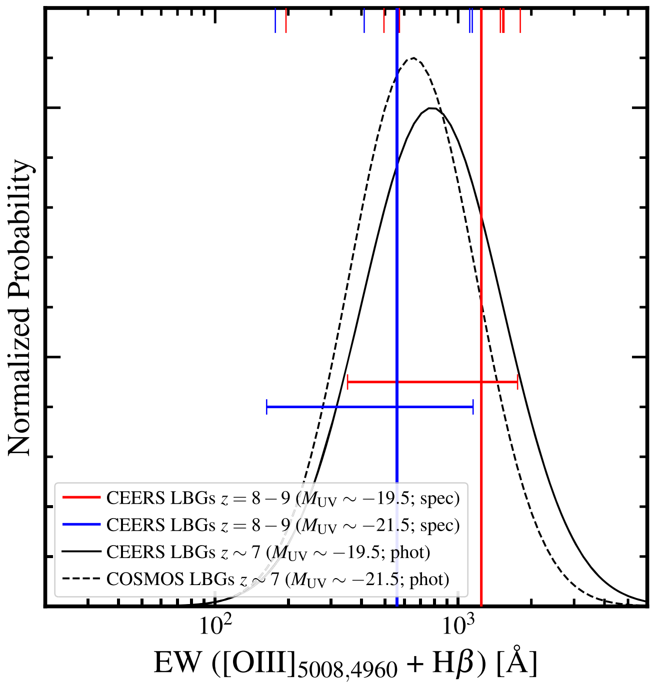

Figure 6. Rest-frame EW distribution of [O III]+Hβ. The red and blue lines and error bars present the median and 16th–84th percentiles of fainter (NIRCam-selected) and brighter (HST-selected; R. Larson et al. 2023, in preparation) LBGs with spectroscopic redshifts $z = 8 - 9$, where the red and blue vertical bars at the top show the individual measurements. The black solid and dashed curves show the best-fit log-normal distribution estimated from SED analysis for photometric samples of 36 luminous LBGs at $z \simeq 6.6 - 6.9$ identified in the COSMOS field ($M_{\rm UV} \sim 21.5$ mag) and 118 less luminous LBGs at $z \sim 6.5$–8 in CEERS (Endsley et al. 2023).

and show the median and 16th–84th percentile of [O III]+Hβ EW values for a sample of brighter HST-selected LBGs in CEERS (blue line and bar), also spectroscopically confirmed at $z = 8 - 9$ (R. Larson et al. 2023, in preparation). The 16th–84th percentile is estimated by assuming a log-normal probability distribution for the EW measurements of each source and summing them to define the entire probability distribution. The upper limits of Hβ EW (MPT-ID2, ID4) are also included in this calculation, assuming that zero and the 3σ error correspond to its center and standard deviation of the log-normal distribution. For comparison, we also present the EW distribution estimated from the photometric-based SED analysis for LBGs at $z \sim 7$ with similar UV luminosity ($M_{\rm UV} \sim -19.5$; solid line) with JWST data and brighter LBGs ($M_{\rm UV} \sim -21.5$; dashed line) at $z \sim 7$ (Endsley et al. 2023).

We obtain median EW([O III]+Hβ) values of 1100^{+560}_{-730}Å and 570^{+590}_{-410}Å for the spec-z confirmed, NIRCam-selected, and HST-selected luminous galaxies, respectively. These measurements are generally much higher than $z = 1 - 4$ galaxies with similar SFR ($\simeq$100–200 Å; Reddy et al. 2018), but consistent with the previous photometric-based measurements for $z = 7 - 8$ galaxies ($\simeq$600–800 Å; e.g., Labbé et al. 2013; De Barros et al. 2019; Endsley et al. 2021). We find that less luminous galaxies have higher EW([O III]+Hβ) values, while the difference is still consistent within the 1σ ranges. The slight increase of EW([O III]+Hβ) in less luminous galaxies agrees with the trend observed in the recent photometric-based results (solid and dashed curves). The increasing trend of EW([O III]+Hβ) with decreasing metallicity has been observed at $z = 1 - 4$ (Reddy et al. 2018). However, in extremely metal-poor systems, the [O III] emission should be suppressed due to the low oxygen abundance, and the EW([O III]+Hβ) value should be significantly smaller for a given value of the ionization parameter. Therefore, the slight increase of EW([O III]+Hβ) observed in our NIRCam-selected galaxies at $z = 8 - 9$ would indicate that these less luminous galaxies are more metal-poor systems than the luminous galaxies, but not extremely metal-poor systems. The high EW([O III]+Hβ) value might also indicate a higher ionization parameter. Recent studies report the detection of the intense nebular emission from highly ionized carbon in the rest-frame UV from $z > 7$ galaxies (Stark et al. 2015, 2017; Laporte et al. 2017; Schmidt et al. 2017; Mainali et al. 2018; Hutchison et al. 2019). From a deep IRAC 5.8 μm band stacking for $z \sim 8$ LBGs, Stefanon et al. (2022) report a large Hα+[N II]EW and subsequently derive a very high ionizing photon production efficiency of $\log(\xi_{\rm ion}/{\rm Hz\,erg}^{-1})$ $=25.97^{+0.18}_{-0.28}$. The redshift evolution of the electron density has also been reported, reaching $n_{\rm e} \gtrsim 300$ cm^{-3} at $z \sim 9$ (Isobe et al. 2023). These results suggest that the ISM in higher-redshift, younger galaxies is more highly ionized than that in lower-z galaxies, which may lead to maintaining the high EW([O III]+Hβ) distribution even in our NIRCam-selected less luminous galaxies at $z = 8 - 9$. We caution that our results might be biased toward the high EW systems, given the fact that the spec-z of high EW systems is easily confirmed via bright emission lines, although our $z_{\rm spec}$ sample represents $\simeq$90% of the less luminous LBGs at $z_{\rm phot} = 8.6 - 9.6$ from the homogeneous selection (Section 4.1). The presence or absence of the increasing trend of EW([O III]+Hβ) distribution as a function of UV luminosity and redshift will be further investigated with larger spectroscopic samples in a separate paper.

4.2.3. *Ionizing Photon Production Efficiency*

To place our $z_{\rm spec}$ sample in the context of cosmic reionization, we also estimate the production efficiency of ionizing photons, $\xi_{\rm ion}$. We measure the $\xi_{\rm ion}$ values via the Balmer recombination line approach (e.g., Bouwens et al. 2016) based on the Hβ line in the same manner as Matthee et al. (2022a) by assuming a zero escape fraction of ionizing photons. A correction for dust attenuation is applied based on our SED fitting results (Section 3.5). For comparison, we measure $\xi_{\rm ion}$ also for the $z_{\rm spec}$ confirmed HST-selected, luminous LBGs (R. Larson et al. 2023, in preparation) in the same manner.

In Figure 7, we show our $\xi_{\rm ion}$ estimates with recent spectroscopic results in different galaxy populations at high redshifts (Stark et al. 2015, 2017; Matthee et al. 2017, 2022a; Tang et al. 2019; Maseda et al. 2020; Atek et al. 2023; Naidu et al. 2022a; Prieto-Lyon et al. 2023) and the canonical value that has been used when modeling the contributions of galaxies to the cosmic reionization (e.g., Robertson et al. 2013). To perform a statistical comparison, we present the median and 16th–84th percentile as the error bar for our $\xi_{\rm ion}$ estimates of our $z_{\rm spec}$ sample by assuming a log-normal probability distribution for the $\xi_{\rm ion}$ measurement of each source. Upper limits for Hβ line fluxes (MPT-ID2, ID4) are also included by assuming that the canonical value and ±0.1 correspond to its center and standard deviation of the log-normal distribution, respectively. We obtain $\log(\xi_{\rm ion}/{\rm Hz\,erg}^{-1})$ $= 25.77^{+0.50}_{-0.43}$ and $25.47^{+0.33}_{-0.23}$ for the NIRCam- and HST-selected sources, respectively. We find that these median $\xi_{\rm ion}$values in our

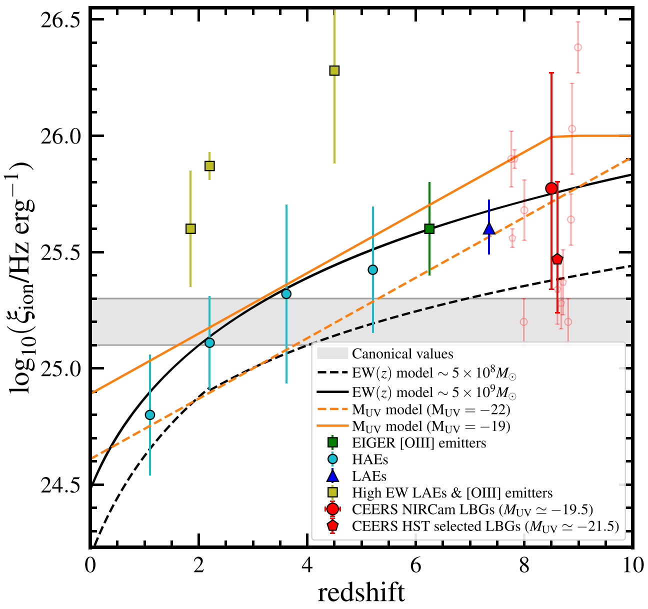

Figure 7. Redshift evolution of the ionizing photon production efficiency $\xi_{\rm ion}$. The red-filled circle and pentagon with error bars present the median and 16th–84th percentiles of the spec-z-confirmed, less luminous, and luminous LBGs at $z = 8 - 9$ selected by NIRCam and HST (R. Larson et al. 2023, in preparation), respectively, where the small, light red open symbols show the individual measurements. Other color symbols are taken or calculated from the literature based on spectroscopy, showing the median or average values for a variety of populations: [O III] emitters at $z \sim 6$ (green squares; Matthee et al. 2022a), Lyα emitters (LAEs) at $z \sim 7$ (blue triangle; Stark et al. 2015, 2017), Hα emitters at $z \sim 1 - 2$ (HAEs, cyan circles; Matthee et al. 2017; Atek et al. 2023; Prieto-Lyon et al. 2023), and LAEs and [O III] emitters with high EWs (deep yellow squares; Tang et al. 2019; Maseda et al. 2020; Naidu et al. 2022a). The gray shade shows the canonical value (e.g., Robertson et al. 2013), and the dashed and solid curves are predictions from empirical models based on Hα EW (black curves; Faisst et al. 2016; Matthee et al. 2017) and UV luminosity (orange curve; Finkelstein et al. 2019).

sample are much higher than the measurements at $z \sim$ 1–2 and the canonical value, but consistent with the recent result for the [O III] emitters (green square) and Lyα emitters (blue triangle) at $z \sim 6 - 7$, and the strong line-emitting galaxies at $z \sim 2 - 4$ (yellow squares). Our results are also consistent with the deep IRAC 5.8 μm band stacking results for $z \sim 8$ LBGs ($25.97^{+0.18}_{-0.28}$; Stefanon et al. 2022). We also find that the less luminous, NIRCam-selected galaxies have higher $\xi_{\rm ion}$ than that of HST-selected galaxies. Although these two measurements are consistent within the 1σ ranges, this trend also aligns with the empirical redshift evolution models, which show increasing $\xi_{\rm ion}$ with increasing mass (black curves; Faisst et al. 2016; Matthee et al. 2017) and UV luminosity (orange curves; Finkelstein et al. 2019), suggesting that faint galaxies play a key role in cosmic reionization.

As discussed in previous studies (e.g., Finkelstein et al. 2019; Matthee et al. 2022a; Stefanon et al. 2022), the $\xi_{\rm ion}$ estimates higher than the canonical values require the modest ($\ll$20%) escape fractions of ionizing photons (e.g., Davies et al. 2021) or that the contribution from faint galaxies ($M_{\rm UV} > -17$; e.g., Matthee et al. 2022b) is minor. Albeit the small statistics, our $z_{\rm spec}$ sample represents the majority ($\simeq$90%) of the LBGs at $z_{\rm phot} = 8.6 - 9.6$ (Section 4.1), which may support the arguments of the modest escape fraction or the negligible contribution from further faint galaxies. However, the high $\xi_{\rm ion}$ measurements observed in galaxies $z \gtrsim 6$ are challenging to the current physics-based galaxy formation models (e.g., Wilkins et al. 2016; Yung et al. 2020b) with standard model components (e.g., power-law IMFs and simple stellar population SEDs). A top-heavy IMF and metal-free star SED in galaxies at these epochs are potential explanations to account for this discrepancy (e.g., Zackrisson et al. 2011; Trussler et al. 2022). Together with the faint-end measurements of the UVLFs at $z > 8$, the contribution of the faint LBG populations to the cosmic reionization, and relevant physical mechanisms, will also be further investigated in separate papers.

4.2.4. Chemical Evolution

The rest-frame optical emission lines have been the most intensively calibrated and widely exploited to constrain the metallicity in distant galaxies (see Maiolino & Mannucci 2019 for a recent review). Our NIRSpec observations cover the wavelength of the key optical emission lines of [O III]5008, Hβ, and [O II] 3727. However, we do not securely detect any [O II] lines from our $z_{\rm spec}$ sample. We thus focus on the R3 ([O III]/Hβ) measurement to examine the oxygen abundance in the following analysis, assuming a negligible contribution from [O II]. The general agreement in the metallicity measurement between the R3-based method and the direct electron temperature method has been confirmed even at $z = 5 - 8$ galaxies in recent JWST studies based on the successful aural [O III]4363 line detection (e.g., Curti et al. 2023; Matthee et al. 2022a).

In the left panel of Figure 8, we show our R3 measurements as a function of $M_{\rm star}$. We also measure and show the HST-selected, luminous LBGs (R. Larson et al. 2023, in preparation) in the same manner.[38] These NIRCam- and HST-selected samples enlarge the $M_{\rm star}$ parameter space and provide a unique opportunity to examine the mass–metallicity relation in a fair manner, owing to the homogeneous sample selection and follow-up sensitivity. For comparison, we also present the recent results for field galaxies at $z = 2 - 3$ (Sanders et al. 2020; Papovich et al. 2022), and $z = 5 - 7$ (Matthee et al. 2022a), and lensed galaxies at $z = 7.5 - 9.5$ (Heintz et al. 2022; Trump et al. 2023; Williams et al. 2023; Mascia et al. 2023). By implication, the R3–$M_{\rm star}$ relation at $z = 2$ is extrapolated, by converting the $z = 2$ mass–metallicity relation (Sanders et al. 2020) based on the R3–metallicity calibration presented in Nakajima et al. (2022). We also show predictions from cosmological galaxy evolution models, incorporating the nebular emission line (Nelson et al. 2019; Yung et al. 2019b, 2022; Hirschmann et al. 2022; Wilkins et al. 2023, 2022).

First, we find in our NIRCam- and HST-selected samples that there is a potential increasing trend in R3 with increasing $M_{\rm star}$. This trend is different from the results at $z \sim 2 - 3$ (black squares) but generally consistent with the model predictions (color-shaded regions), where the increasing trend is explained by the high ionization parameter in early galaxies (Hirschmann et al. 2022; M. Hirschmann et al. 2023, in preparation). High O32 values of $\gtrsim$10 have been reported from the composite spectrum for $z \sim$ 7.5–8.0 galaxies (Cameron et al. 2023; Sanders et al. 2023; Tang et al. 2023), which also suggests the highly ionized ISM state in early galaxies. Second, we compare our measurements with recent JWST results and find that our NIRCam-selected galaxies show the R3–$M_{\rm star}$ distribution similar to the lensed galaxies at $z = 7.5 - 9.5$,

---

[38] One of the CEERS HST-selected galaxies, MPT-ID (1019), shows several possible AGN features (Larson et al. 2023), and thus we do not include MPT-ID (1019) in this analysis.

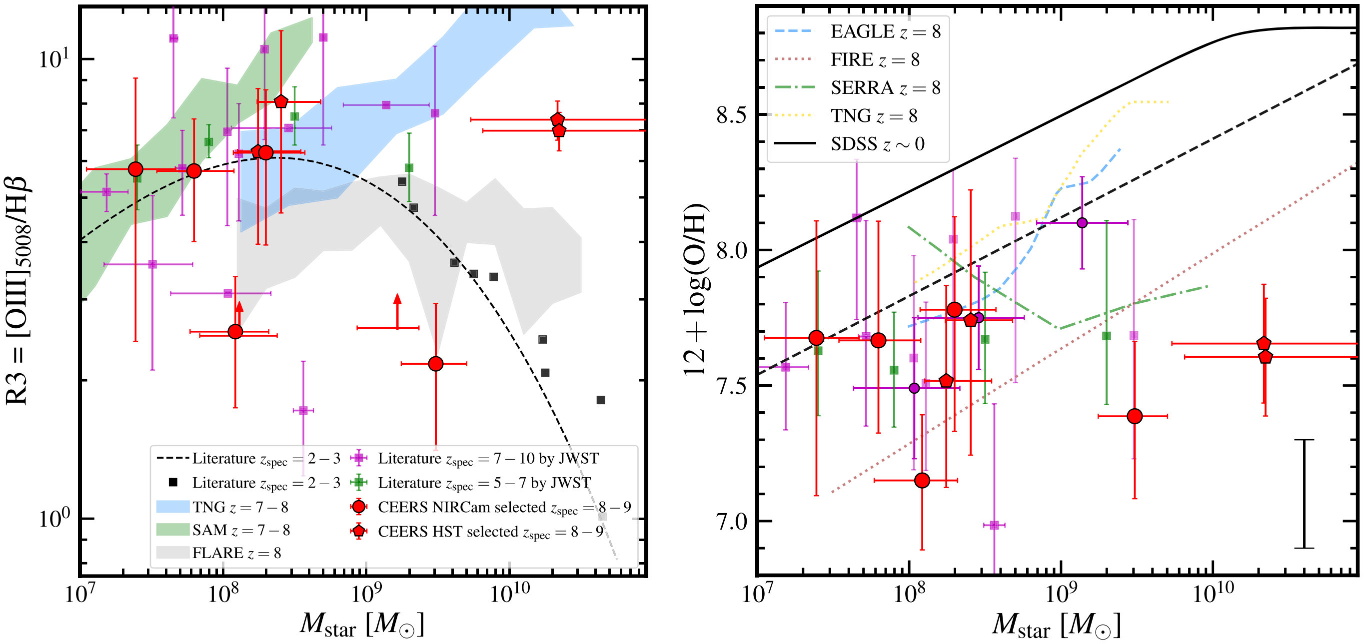

Figure 8. Left: R3 vs. $M_{\rm star}$ relation. The red circles and pentagons present our NIRCam- and HST-selected galaxies at $z = 8 - 9$ in CEERS, respectively, including lower limits. The magenta and green squares denote the recent JWST results for lensed galaxies at $z = 7.5$–9.5 (Heintz et al. 2022; Trump et al. 2023; Williams et al. 2023; Mascia et al. 2023), and general field galaxies at $z = 5 - 7$ (Matthee et al. 2022a). The black squares show the results for general field galaxies at $z \sim 2 - 3$ (Sanders et al. 2020; Papovich et al. 2022), where its R3–$M_{\rm star}$ relation is extrapolated by converting the mass–metallicity relation based on the R3 calibration of Nakajima et al. (2022). The color-shaded area indicates the 16th–84th percentile of simulated galaxies at $z = 7 - 8$ in TNG50 and TNG100 (e.g., Nelson et al. 2019) and Santa Cruz SAM (e.g., Yung et al. 2019b, 2022), incorporating the nebular emission line calculations (Hirschmann et al. 2022), and FLARE (Wilkins et al. 2023, 2022). Right: metallicity vs. $M_{\rm star}$ relation. Our and other R3 measurements at $z > 7$ are shown in the left panel, converted using the R3–metallicity calibration, where the typical error scale from different calibrations is represented by the black bar in the lower right corner (see text). The black lines are the best-fit relation at $z = 0$ (solid), and $z = 3$ (dashed; Sanders et al. 2021), while the other color lines denote the predictions from simulations (Schaye et al. 2015; Ma et al. 2016; Pallottini et al. 2022; Ucci et al. 2023). The magenta circles are the measurements based on the [O III]4363 line for three lensed galaxies at $z = 7.7$–8.5 (e.g., Curti et al. 2023; Schaerer et al. 2022; Trump et al. 2023). The mass–metallicity relation at $z = 8 - 9$ is likely placed below the relations at $z = 0 - 3$ which is generally consistent with the predictions from simulations.

ranging over the R3 values of ∼2–6 that are generally comparable or lower than those of the field galaxies, at $z = 5 - 7$. Below 12+log(O/H) ≈ 8, the R3 values generally decrease toward low metallicity because the [O III] emission is suppressed in the low oxygen abundance (e.g., Maiolino et al. 2008; Curti et al. 2017; Bian et al. 2018; Nakajima et al. 2022). Thus, the lower R3 values in galaxies from CEERS and lensing samples at $z \gtrsim 8$ with respect to the $z = 5 - 7$ field galaxies might indicate a decreasing metallicity trend at a given $M_{\rm star}$ toward high redshifts. Although a few sources are placed much below the other sources and the model predictions at $\log(M_{\rm star}/M_\odot) \gtrsim 8.5$, this might indicate that the pristine gas inflow might be taking place in these exceptional galaxies, which maintains the oxygen abundance low and makes their [O III] line emissivity very low.

In the right panel of Figure 8, we present the metallicity measurements at $z = 0 - 9$. We estimate the metallicities of our sample using the R3 calibration of Nakajima et al. (2022) that takes Hβ EW (≈ionization state) into account and expands the calibration down to $12 + \log({\rm O/H}) \simeq 6.9$ by analyzing the local extremely metal-poor galaxies.[39] We obtain $12 + \log({\rm O/H}) \simeq 7.2 - 7.8$ for the NIRCam-selected galaxies at $z = 8 - 9$. These estimates typically change by ∼0.4, if we use another calibration of Bian et al. (2018). Some HST-selected galaxies exhibit high R3 values (>6) that surpass the possible range in the calibration mentioned above. In such cases, we employ an alternative calibration for simulated galaxies at $z = 4 - 8$ (Hirschmann et al. 2022; M. Hirschmann et al. 2023, in preparation)[40] that reproduces the increasing R3 trend with increasing $M_{\rm star}$ in the left panel. This yields $12 + \log({\rm O/H}) \simeq 7.6 - 8.2$ for the HST-selected galaxies. Based on these calibrations, we find that the galaxies at $z = 8 - 9$ fall below the mass–metallicity relations, at $z = 0 - 3$ (e.g., Sanders et al. 2021) extrapolated down to $M_{\rm star} \sim 10^7\,M_\odot$. This is generally consistent with the model predictions (e.g., Schaye et al. 2015; Ma et al. 2016; Pallottini et al. 2022; Ucci et al. 2023) and the recent JWST results of the mass–metallicity measurements at $z = 5 - 9.5$ (Heintz et al. 2022; Langeroodi et al. 2022; Matthee et al. 2022a), but with different calibrations (e.g., Bian et al. 2018; Curti et al. 2020). By applying the R3 calibrations to these recent JWST results in the same manner as above, we obtain $12 + \log({\rm O/H}) \simeq 7.7 - 8.1$ and ≃7.5 − 7.8 for the $z = 5 - 7$ field galaxies, and the lensed galaxies at $z = 6.9 - 8.1$, respectively. This implies that the metallicity of our NIRCam-selected galaxies at $z = 8 - 9$ is consistent with the recent JWST results within the large scatter. Combined with our SFR–$M_{\rm star}$ results (Section 4.2.1), we find that galaxies at $\log(M_{\rm star}/M_\odot) \simeq 8 - 9$ have a trend of an

---

[39] For the sources with EW(Hβ) > 150 Å and the other, we use the R3–metallicity conversion calibrated for high ($\gtrsim$200 Å) and low ($\lesssim$100 Å) Hβ EW sources in Nakajima et al. (2022), respectively. In this conversion, we assume that our NIRCam-selected sample has $12 + \log({\rm O/H}) \leqslant 8.2$, because of their less massive properties ($\lesssim 10^9 M_\odot$; see Figure 5) and lower limit of O32 (Table 2) that correspond to a low oxygen abundance of $12 + \log({\rm O/H}) \lesssim 8.2$ based on the O32 calibration (e.g., Maiolino et al. 2008; Curti et al. 2017; Bian et al. 2018; Pérez-Montero et al. 2021; Casey et al. 2022; Nakajima et al. 2022).

[40] $R3 = P0 + P1 * x + P2 * x^2$, where $P0 = -14.424$, $P1 = 3.521$, $P2 = -0.199$, and $x = 12 + \log({\rm O/H})$.

increasing SFR and decreasing metallicity from $z \sim 2-6$ to $z \sim 8-9$.

5. Summary

In this paper, we present JWST NIRSpec MOS results for 11 high-redshift galaxy candidates at $z \gtrsim 8.5$ selected from deep NIRCam data taken in 2022 June in the Cosmic Evolution Early Release Science (CEERS) field. All targets are observed with the prism or medium-resolution G140M/F100LP, G235M/F170LP, and G395M/F290LP gratings, both of which continuously cover ∼1–5 μm wavelengths in the observed frame, maximizing the chance of spectroscopic confirmation by either emission lines or the Lyα break. This is the first homogeneous, luminosity-selected follow-up JWST spectroscopy for high-redshift galaxy candidates selected with NIRCam in the UV luminosity range of $M_{\rm UV} \in [-21, -18]$, setting the benchmark for future high-redshift galaxy selection at $z \gtrsim 8.5$ with NIRCam. Comparing with the HST-selected luminous ($M_{\rm UV} \simeq -22$) galaxies that are also spectroscopically confirmed at similar redshifts (R. Larson et al. 2023, in preparation), we also investigate the characteristics of these NIRCam-selected galaxies. The main findings of this paper are summarized as follows:

1. We systematically analyze 1D and 2D spectra and spectroscopically confirm 7 out of 11 targets with [O III]5008, 4960 lines at $z = 7.762-8.998$. One of the candidates shows a potential single-line detection at 5.20 μm, which may indicate the galaxy redshift at $z = 9.386$, or $z = 9.697$, depending on whether the line is [O III]5008 or Hβ. We do not detect emission lines or Lyα continuum breaks in the other three candidates.
2. Based on the original $z_{\rm phot}$ estimate, the success ratio of the spec-z confirmation for $z_{\rm phot} = 8.5-9.6$ candidates reaches $\simeq$90% (=6/7). The absence of robust multiple-line identifications in three out of four $z_{\rm phot} > 10$ candidates might indicate that strong optical emission lines (e.g., [O III]5008, Hβ) in these galaxies are redshifted beyond the NIRSpec wavelength range, and may support a high purity also in the $z_{\rm phot} > 10$ candidate selection. The spec-z confirmation results from the homogeneous sample selection and follow-up observations are widely useful to interpret the UV luminosity function studies now explored out to $z \sim 17$ with JWST/NIRCam.
3. Although all $z_{\rm spec}$ values fall within the 95% confidence interval of the original $z_{\rm phot}$ estimates, we find the majority of the sources show $z_{\rm spec} < z_{\rm phot}$, where almost half exceed the 68% confidence interval. This may indicate that the galaxy templates generally used for high-redshift galaxy selection at $z \gtrsim 8.5$ are still insufficient to recover their rest-frame UV color space. This could also be caused by the possible limitations inherent in using a single photo-z code, the lack of a deep NIRCam dropout filter (e.g., F090W), or the potential bias due to the fact that the strong line identification is limited to $z \lesssim 9.5$.
4. We perform the SED fitting to the HST+NIRCam photometry and [O III]5008 EW and evaluate the SFR and stellar mass ($M_{\rm star}$) relation for the seven spec-z confirmed sources. The typical SFR and $M_{\rm star}$ are estimated to be $\simeq 4\,M_\odot$ yr^{-1} and $\simeq 10^8\,M_\odot$. This yields a relatively high specific SFR of $\simeq$40 Gyr^{-1} compared to the main sequence at $z = 2-6$.
5. We measure the rest-frame [O III]+Hβ EW and obtain median values of 1100^{+560}_{-730} Å and 570^{+590}_{-410} Å for our NIRCam- and HST-selected galaxies spectroscopically confirmed at $z = 8-9$, respectively. This is much higher than typical star-forming galaxies at $z \sim 1-2$ but consistent with previous photometric-based results at $z \sim 7$ in a similar UV luminosity range. The potential larger EW([O III]+Hβ) value in the NIRCam-selected galaxies may indicate these less luminous galaxies are not extremely metal-poor, but less metal-enriched systems with more ionizing photons maintaining the EW([O III]+Hβ) slightly higher than the UV-luminous HST-selected galaxies.
6. We also evaluate $\xi_{\rm ion}$ and find that our NIRCam- and HST-selected galaxies have median values of $\log(\xi_{\rm ion}/{\rm Hz\,erg^{-1}}) = 25.77^{+0.50}_{-0.43}$ and $25.47^{+0.33}_{-0.23}$, respectively, at $z_{\rm spec} = 8-9$. These median estimates are much higher than those from typical star-forming galaxies at $z \sim 1-2$ but consistent with the recent measurements for the [O III] emitters and Lyα emitters at $z = 5-7$. The potential trend toward higher $\xi_{\rm ion}$ in less luminous galaxies indicates the important contributions from faint galaxies to the cosmic reionization, which is consistent with the empirical model predictions based on Hα EW and UV luminosity.
7. We analyze the [O III]/Hβ line ratio ≡ R3 as a function of $M_{\rm star}$ for the NIRCam- and HST-selected galaxies. We find an increasing trend of R3 toward high $M_{\rm star}$. This trend is opposite to the $z \sim 2-3$ results, while it is consistent with the predictions from the simulations because of the high ionization parameter in the early galaxies. With an empirical calibration of the R3 method, we evaluate the oxygen abundance and find that these $z = 8-9$ galaxies have lower metallicity, than that of $z = 0-3$ galaxies at a given $M_{\rm star}$. This is generally consistent with the current galaxy formation and evolution models.

We thank Gabriel Brammer for sharing insights into the NIRSpec data analysis and Takashi Kojima and Ryan Endsley for useful discussions for this paper. We thank the entire CEERS team for their effort to design and execute this observational program, especially the work to design the MSA observations. This work is based on observations with the NASA/ESA/Canadian Space Agency (CSA) James Webb Space Telescope obtained from the Mikulski Archive for Space Telescopes at the STScI, which is operated by the Association of Universities for Research in Astronomy (AURA), Incorporated, under NASA contract NAS5-03127. We acknowledge support from NASA through STScI ERS award JWST-ERS-1345. This research also made use of the NASA/IPAC Infrared Science Archive (IRSA), which is operated by the Jet Propulsion Laboratory, California Institute of Technology, under contract with the National Aeronautics and Space Administration. This project has received funding from NASA through the NASA Hubble Fellowship grant HST-HF2-51505.001-A awarded by the Space Telescope Science Institute, which is operated by the Association of Universities for Research in Astronomy, Incorporated, under NASA contract NAS5-26555.

Some or all of the data presented in this paper were obtained from the Mikulski Archive for Space Telescopes (MAST) at

the Space Telescope Science Institute. The specific observations analyzed can be accessed via doi:10.17909/z7p0-8481.

Software: `Astropy` (Astropy Collaboration et al. 2013), `CIGALE` (Boquien et al. 2019), `Mosviz` (Developers et al. 2023).

Appendix A
Sources without Spectroscopic Redshift Confirmation

In Figures 9 and 10, we show the 1D+2D spectra for the sources that are not spectroscopically confirmed in this study.

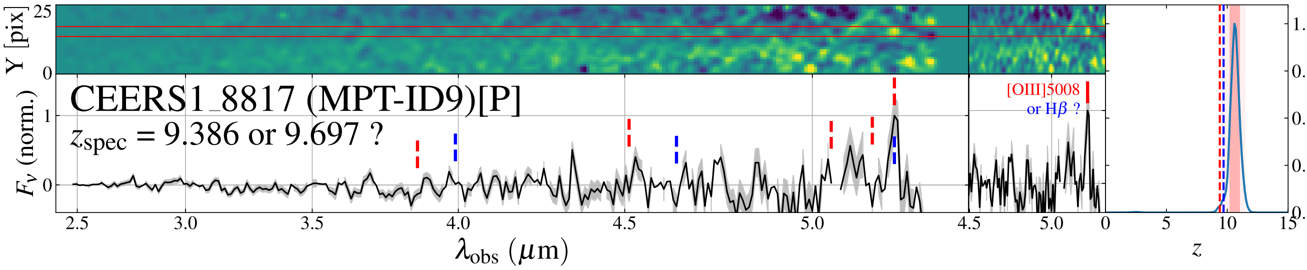

Figure 9. Same as Figure 2, but for MPT-ID9 with the potential single-line detection at 5.20 μm. The red and blue vertical lines indicate the expected wavelengths for the [O III]5008, [O III]4969, Hβ, Hγ, and [O II]3727, from right to left when the 5.20 μm line feature corresponds to [O III]5008 and Hβ, respectively. For the potential line, we rule out the possibility of [O III]4960, because the 3× more bright [O III]5008 line should be detected at the edge of the spectrum in this case. The [O II]3727 at $z = 12.95$ is also unlikely based on the photometric redshift $P(z)$.

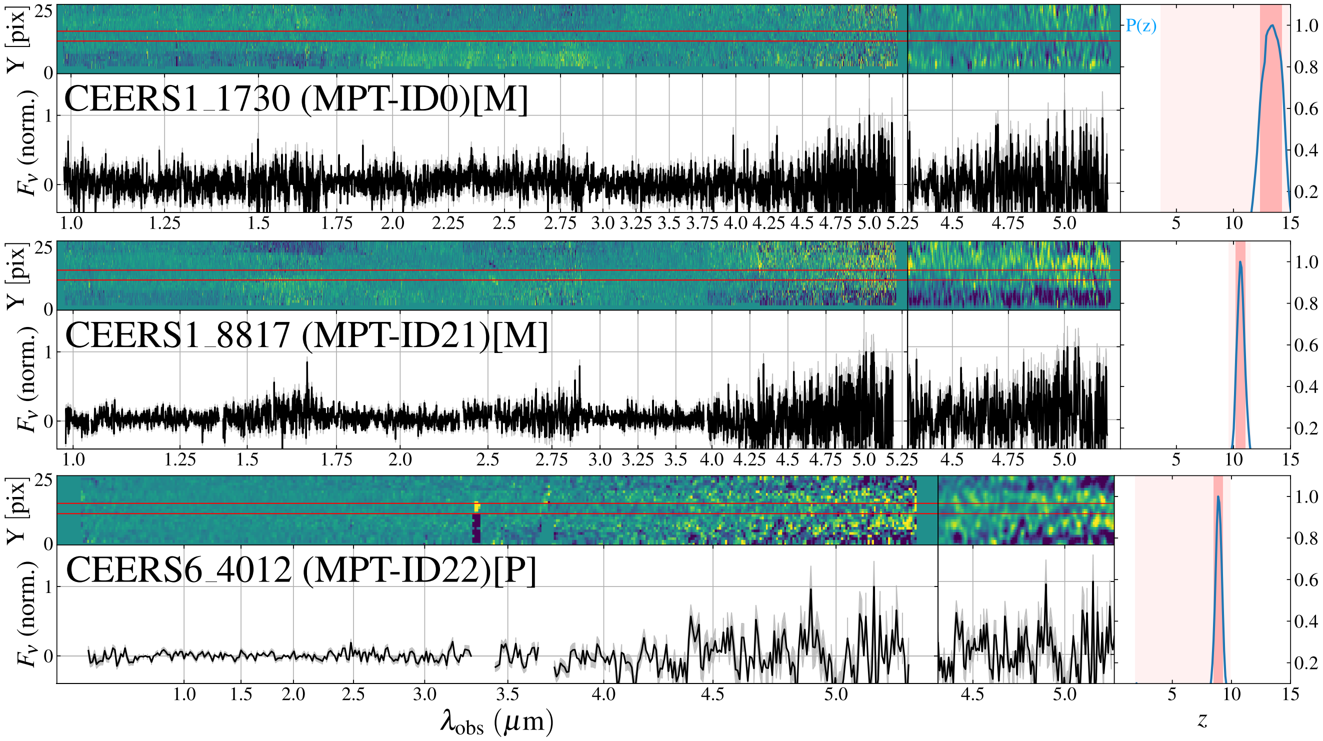

Figure 10. Same as Figure 2, but for MPT-ID0, ID21, and ID22 without a robust line or continuum detection.

Appendix B
Continuum Break

In Figure 11, we show the 1D+2D prism spectrum for MPT-ID7 in the spectral region around 1 μm. We detect continuum emission at $\lambda \gtrsim 1.2\,\mu$m consistent with expectations for the Lyα break at the redshift determined from the [O III] and Hβ emission lines.

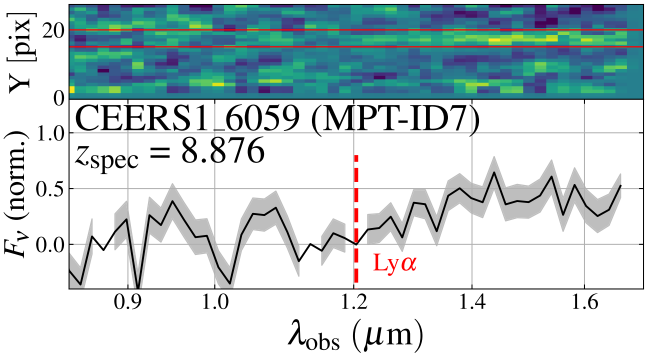

Figure 11. Same as Figure 2, but zoomed at around ∼1 μm of MPT-ID7 whose Lyα continuum break is identified in the 1D and 2D spectra. The wavelength of the continuum break is consistent with the emission-line-determined spectroscopic redshift.

Appendix C
Best-fit SED

In Figure 12, we show our best-fit SED model for MPT-ID2 by using CIGALE as an example. A comprehensive list and further details of the SED models will be provided in D. Burgarella et al. (in preparation).

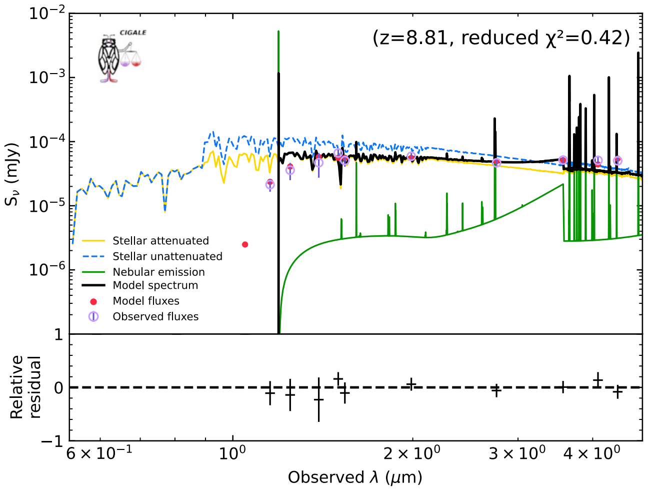

Figure 12. Best-fit SED for MPT-ID2 modeled with CIGALE. Colored curves represent the emission from the various components described in the label, with the black curve representing their sum. Magenta and red circles indicate the observed and model-predicted fluxes in the NIRCam broadband filters, respectively.

ORCID iDs

Seiji Fujimoto https://orcid.org/0000-0001-7201-5066
Pablo Arrabal Haro https://orcid.org/0000-0002-7959-8783
Mark Dickinson https://orcid.org/0000-0001-5414-5131
Steven L. Finkelstein https://orcid.org/0000-0001-8519-1130
Jeyhan S. Kartaltepe https://orcid.org/0000-0001-9187-3605
Rebecca L. Larson https://orcid.org/0000-0003-2366-8858
Denis Burgarella https://orcid.org/0000-0002-4193-2539
Micaela B. Bagley https://orcid.org/0000-0002-9921-9218
Peter Behroozi https://orcid.org/0000-0002-2517-6446
Katherine Chworowsky https://orcid.org/0000-0003-4922-0613
Michaela Hirschmann https://orcid.org/0000-0002-3301-332
Jonathan R. Trump https://orcid.org/0000-0002-1410-0470
Stephen M. Wilkins https://orcid.org/0000-0003-3903-6935
L. Y. Aaron Yung https://orcid.org/0000-0003-3466-035X
Anton M. Koekemoer https://orcid.org/0000-0002-6610-2048
Casey Papovich https://orcid.org/0000-0001-7503-8482
Nor Pirzkal https://orcid.org/0000-0003-3382-5941
Henry C. Ferguson https://orcid.org/0000-0001-7113-2738
Adriano Fontana https://orcid.org/0000-0003-3820-2823
Norman A. Grogin https://orcid.org/0000-0001-9440-8872
Andrea Grazian https://orcid.org/0000-0002-5688-0663
Lisa J. Kewley https://orcid.org/0000-0001-8152-3943
Dale D. Kocevski https://orcid.org/0000-0002-8360-3880
Jennifer M. Lotz https://orcid.org/0000-0003-3130-5643
Laura Pentericci https://orcid.org/0000-0001-8940-6768
Swara Ravindranath https://orcid.org/0000-0002-5269-6527
Rachel S. Somerville https://orcid.org/0000-0002-6748-6821
Stephen M. Wilkins https://orcid.org/0000-0003-3903-6935
Ricardo O. Amorín https://orcid.org/0000-0001-5758-1000
Bren E. Backhaus https://orcid.org/0000-0001-8534-7502
Antonello Calabrò https://orcid.org/0000-0003-2536-1614
Caitlin M. Casey https://orcid.org/0000-0002-0930-6466
M. C. Cooper https://orcid.org/0000-0003-1371-6019
Vital Fernández https://orcid.org/0000-0003-0531-5450
Maximilien Franco https://orcid.org/0000-0002-3560-8599
Mauro Giavalisco https://orcid.org/0000-0002-7831-8751
Nimish P. Hathi https://orcid.org/0000-0001-6145-5090
Santosh Harish https://orcid.org/0000-0003-0129-2079
Taylor A. Hutchison https://orcid.org/0000-0001-6251-4988
Kartheik G. Iyer https://orcid.org/0000-0001-9298-3523
Intae Jung https://orcid.org/0000-0003-1187-4240
Ray A. Lucas https://orcid.org/0000-0003-1581-7825
Jorge A. Zavala https://orcid.org/0000-0002-7051-1100

References

Adams, N. J., Conselice, C. J., Ferreira, L., et al. 2023, MNRAS, 518, 4755
Amorín, R., Fontana, A., Pérez-Montero, E., et al. 2017, NatAs, 1, 0052
Arrabal Haro, P., Dickinson, M., Finkelstein, S. L., et al. 2023a, arXiv:2304.05378
Arrabal Haro, P., Dickinson, M., Finkelstein, S. L., et al. 2023b, arXiv:2303.15431
Astropy Collaboration, Robitaille, T. P., Tollerud, E. J., et al. 2013, A&A, 558, A33
Atek, H., Shuntov, M., Furtak, L. J., et al. 2023, MNRAS, 519, 1201
Bagley, M. B., Finkelstein, S. L., Koekemoer, A. M., et al. 2023, ApJL, 946, L12
Bakx, T. J. L. C., Zavala, J. A., Mitsuhashi, I., et al. 2023, MNRAS, 519, 5076
Behroozi, P., Conroy, C., Wechsler, R. H., et al. 2020, MNRAS, 499, 5702

Behroozi, P., Wechsler, R. H., Hearin, A. P., & Conroy, C. 2019, MNRAS, 488, 3143

Behroozi, P. S., & Silk, J. 2015, ApJ, 799, 32

Behroozi, P. S., Wechsler, R. H., & Conroy, C. 2013, ApJ, 770, 57

Beichman, C. A., Rieke, M., Eisenstein, D., et al. 2012, Proc. SPIE, 8442, 84422N

Bhatawdekar, R., Conselice, C. J., Margalef-Bentabol, B., & Duncan, K. 2019, MNRAS, 486, 3805

Bian, F., Kewley, L. J., & Dopita, M. A. 2018, ApJ, 859, 175

Boquien, M., Burgarella, D., Roehlly, Y., et al. 2019, A&A, 622, A103

Bouwens, R., Illingworth, G., Oesch, P., et al. 2023a, MNRAS, Advance Access

Bouwens, R. J., Illingworth, G. D., Oesch, P. A., et al. 2015, ApJ, 803, 34

Bouwens, R. J., Oesch, P. A., Stefanon, M., et al. 2021, AJ, 162, 47

Bouwens, R. J., Smit, R., Labbé, I., et al. 2016, ApJ, 831, 176

Bouwens, R. J., Smit, R., Schouws, S., et al. 2022, ApJ, 931, 160

Bouwens, R. J., Stefanon, M., Brammer, G., et al. 2023b, MNRAS, Advance Access

Boylan-Kolchin, M. 2023, NatAs, Advanced Online Publication

Bradley, L. D., Coe, D., Brammer, G., et al. 2022, arXiv:2210.01777

Brammer, G. B., van Dokkum, P. G., & Coppi, P. 2008, ApJ, 686, 1503

Bunker, A. J., Saxena, A., Cameron, A. J., et al. 2023, arXiv:2302.07256

Burgarella, D., Buat, V., & Iglesias-Páramo, J. 2005, MNRAS, 360, 1413

Calzetti, D., Armus, L., Bohlin, R. C., et al. 2000, ApJ, 533, 682

Cameron, A. J., Saxena, A., Bunker, A. J., et al. 2023, arXiv:2302.04298

Casey, C. M., Kartaltepe, J. S., Drakos, N. E., et al. 2022, arXiv:2211.07865

Castellano, M., Fontana, A., Treu, T., et al. 2022, ApJL, 938, L15

Chabrier, G. 2003, PASP, 115, 763

Conroy, C., & Gunn, J. E. 2010, ApJ, 712, 833

Curti, M., Cresci, G., Mannucci, F., et al. 2017, MNRAS, 465, 1384

Curti, M., D'Eugenio, F., Carniani, S., et al. 2023, MNRAS, 518, 425

Curti, M., Maiolino, R., Cirasuolo, M., et al. 2020, MNRAS, 492, 821

Curtis-Lake, E., Carniani, S., Cameron, A., et al. 2023, NatAs, Advanced Online Publication

Dahlen, T., Mobasher, B., Faber, S. M., et al. 2013, ApJ, 775, 93

Davé, R., Anglés-Alcázar, D., Narayanan, D., et al. 2019, MNRAS, 486, 2827

Davies, R. L., Förster Schreiber, N. M., Genzel, R., et al. 2021, ApJ, 909, 78

Dayal, P., Choudhury, T. R., Bromm, V., & Pacucci, F. 2017, ApJ, 836, 16

De Barros, S., Oesch, P. A., Labbé, I., et al. 2019, MNRAS, 489, 2355

Developers, J., Averbukh, J., Bradley, L., et al. 2023, Jdaviz, v3.2.0, Zenodo, doi:10.5281/zenodo.7504710

Ding, X., Onoue, M., Silverman, J. D., et al. 2022, arXiv:2211.14329

Donnan, C. T., McLeod, D. J., Dunlop, J. S., et al. 2023a, MNRAS, 518, 6011

Donnan, C. T., McLeod, D. J., McLure, R. J., et al. 2023b, MNRAS, 520, 4554

Eldridge, J. J., & Stanway, E. R. 2009, MNRAS, 400, 1019

Eldridge, J. J., Stanway, E. R., Xiao, L., et al. 2017, PASA, 34, e058

Ellis, R. S., McLure, R. J., Dunlop, J. S., et al. 2013, ApJL, 763, L7

Endsley, R., Stark, D. P., Chevallard, J., & Charlot, S. 2021, MNRAS, 500, 5229

Endsley, R., Stark, D. P., Lyu, J., et al. 2023, MNRAS, 520, 4609

Faisst, A. L., Capak, P., Hsieh, B. C., et al. 2016, ApJ, 821, 122

Ferland, G. J., Chatzikos, M., Guzmán, F., et al. 2017, RMxAA, 53, 385

Ferrara, A., Pallottini, A., & Dayal, P. 2023, MNRAS, 522, 3986

Ferruit, P., Jakobsen, P., Giardino, G., et al. 2022, A&A, 661, A81

Finkelstein, S. L., Bagley, M. B., Ferguson, H. C., et al. 2023, ApJL, 946, L13

Finkelstein, S. L., Bagley, M. B., Haro, P. A., et al. 2022, ApJL, 940, L55

Finkelstein, S. L., D'Aloisio, A., Paardekooper, J.-P., et al. 2019, ApJ, 879, 36

Finkelstein, S. L., Ryan, R. E. J., Papovich, C., et al. 2015, ApJ, 810, 71

Fujimoto, S., Finkelstein, S. L., Burgarella, D., et al. 2022a, arXiv:2211.03896

Fujimoto, S., Ouchi, M., Nakajima, K., et al. 2022b, arXiv:2212.06863

Giménez-Arteaga, C., Oesch, P. A., Brammer, G. B., et al. 2023, ApJ, 948, 126

Grogin, N. A., Kocevski, D. D., Faber, S. M., et al. 2011, ApJS, 197, 35

Harikane, Y., Nakajima, K., Ouchi, M., et al. 2023a, arXiv:2304.06658

Harikane, Y., Ouchi, M., Oguri, M., et al. 2023b, ApJS, 265, 5

Heintz, K. E., Brammer, G. B., Giménez-Arteaga, C., et al. 2022, arXiv:2212.02890

Hirschmann, M., Charlot, S., Feltre, A., et al. 2022, arXiv:2212.02522

Hutchison, T. A., Papovich, C., Finkelstein, S. L., et al. 2019, ApJ, 879, 70

Isobe, Y., Ouchi, M., Nakajima, K., et al. 2023, arXiv:2301.06811

Iyer, K., Gawiser, E., Davé, R., et al. 2018, ApJ, 866, 120

Iyer, K. G., Gawiser, E., Faber, S. M., et al. 2019, ApJ, 879, 116

Jakobsen, P., Ferruit, P., Alves de Oliveira, C., et al. 2022, A&A, 661, A80

Kannan, R., Springel, V., Hernquist, L., et al. 2022, arXiv:2210.10066

Khusanova, Y., Le Fèvre, O., Cassata, P., et al. 2020, A&A, 634, A97

Koekemoer, A. M., Faber, S. M., Ferguson, H. C., et al. 2011, ApJS, 197, 36

Labbé, I., Oesch, P. A., Bouwens, R. J., et al. 2013, ApJL, 777, L19

Labbe, I., van Dokkum, P., Nelson, E., et al. 2023, Natur, 616, 266

Langeroodi, D., Hjorth, J., Chen, W., et al. 2022, arXiv:2212.02491

Laporte, N., Nakajima, K., Ellis, R. S., et al. 2017, ApJ, 851, 40

Larson, R. L., Finkelstein, S. L., Kocevski, D. D., et al. 2023, arXiv:2303.08918

Larson, R. L., Hutchison, T. A., Bagley, M., et al. 2022, arXiv:2211.10035

Lovell, C. C., Harrison, I., Harikane, Y., Tacchella, S., & Wilkins, S. M. 2023, MNRAS, 518, 2511

Ma, X., Hopkins, P. F., Faucher-Giguère, C.-A., et al. 2016, MNRAS, 456, 2140

Mainali, R., Zitrin, A., Stark, D. P., et al. 2018, MNRAS, 479, 1180

Maiolino, R., & Mannucci, F. 2019, A&ARv, 27, 3

Maiolino, R., Nagao, T., Grazian, A., et al. 2008, A&A, 488, 463

Mascia, S., Pentericci, L., Calabro', A., et al. 2023, A&A, 672, A155

Maseda, M. V., Bacon, R., Lam, D., et al. 2020, MNRAS, 493, 5120

Mason, C. A., Trenti, M., & Treu, T. 2023, MNRAS, 521, 497

Matthee, J., Mackenzie, R., Simcoe, R. A., et al. 2022a, arXiv:2211.08255

Matthee, J., Naidu, R. P., Pezzulli, G., et al. 2022b, MNRAS, 512, 5960

Matthee, J., Sobral, D., Boone, F., et al. 2017, ApJ, 851, 145

Menci, N., Castellano, M., Santini, P., et al. 2022, ApJL, 938, L5

Morishita, T., & Stiavelli, M. 2023, ApJL, 946, L35

Naidu, R. P., Matthee, J., Oesch, P. A., et al. 2022a, MNRAS, 510, 4582

Naidu, R. P., Oesch, P. A., Setton, D. J., et al. 2022b, arXiv:2208.02794

Naidu, R. P., Oesch, P. A., van Dokkum, P., et al. 2022c, ApJL, 940, L14

Nakajima, K., Ouchi, M., Xu, Y., et al. 2022, ApJS, 262, 3

Nelson, D., Pillepich, A., Springel, V., et al. 2019, MNRAS, 490, 3234

Noll, S., Burgarella, D., Giovannoli, E., et al. 2009, A&A, 507, 1793

Oesch, P. A., Brammer, G., van Dokkum, P. G., et al. 2016, ApJ, 819, 129

Osterbrock, D. E. 1989, Astrophysics of Gaseous Nebulae and Active Galactic Nuclei (Mill Valley, CA: Univ. Science Books)

Pallottini, A., Ferrara, A., Gallerani, S., et al. 2022, MNRAS, 513, 5621

Papovich, C., Cole, J., Yang, G., et al. 2022, arXiv:2301.00027

Pei, Y. C. 1992, ApJ, 395, 130

Pérez-González, P. G., Costantin, L., Langeroodi, D., et al. 2023, arXiv:2302.02429

Pérez-Montero, E., Amorín, R., Sánchez Almeida, J., et al. 2021, MNRAS, 504, 1237

Pontoppidan, K., Blome, C., Braun, H., et al. 2022, ApJ, 936, L14

Prieto-Lyon, G., Strait, V., Mason, C. A., et al. 2023, A&A, 672, A186

Reddy, N. A., Shapley, A. E., Sanders, R. L., et al. 2018, ApJ, 869, 92

Rieke, M. J., Baum, S. A., Beichman, C. A., et al. 2003, Proc. SPIE, 4850, 478

Rieke, M. J., Kelly, D., & Horner, S. 2005, Proc. SPIE, 5904, 1

Rigby, J., Perrin, M., McElwain, M., et al. 2023, PASP, 135, 048001

Roberts-Borsani, G., Treu, T., Chen, W., et al. 2022, arXiv:2210.15639

Robertson, B. E., Furlanetto, S. R., Schneider, E., et al. 2013, ApJ, 768, 71

Robertson, B. E., Tacchella, S., Johnson, B. D., et al. 2023, NatAs, Advanced Online Publication

Sanders, R. L., Shapley, A. E., Jones, T., et al. 2021, ApJ, 914, 19

Sanders, R. L., Shapley, A. E., Reddy, N. A., et al. 2020, MNRAS, 491, 1427

Sanders, R. L., Shapley, A. E., Topping, M. W., Reddy, N. A., & Brammer, G. B. 2023, arXiv:2301.06696

Schaerer, D., Marques-Chaves, R., Oesch, P., et al. 2022, A&A, 665, L4

Schaye, J., Crain, R. A., Bower, R. G., et al. 2015, MNRAS, 446, 521

Schmidt, K. B., Huang, K. H., Treu, T., et al. 2017, ApJ, 839, 17

Speagle, J. S., Steinhardt, C. L., Capak, P. L., & Silverman, J. D. 2014, ApJS, 214, 15

Stark, D. P., Ellis, R. S., Charlot, S., et al. 2017, MNRAS, 464, 469

Stark, D. P., Walth, G., Charlot, S., et al. 2015, MNRAS, 454, 1393

Stefanon, M., Bouwens, R. J., Illingworth, G. D., et al. 2022, ApJ, 935, 94

Tacchella, S., Finkelstein, S. L., Bagley, M., et al. 2022, ApJ, 927, 170

Tacchella, S., Johnson, B. D., Robertson, B. E., et al. 2023, MNRAS, Advance Access

Tacconi, L. J., Neri, R., Genzel, R., et al. 2013, ApJ, 768, 74

Tang, M., Stark, D. P., Chen, Z., et al. 2023, arXiv:2301.07072

Tang, M., Stark, D. P., Chevallard, J., & Charlot, S. 2019, MNRAS, 489, 2572

Tasca, L. A. M., Le Fèvre, O., Hathi, N. P., et al. 2015, A&A, 581, A54

Treu, T., Roberts-Borsani, G., Bradac, M., et al. 2022, ApJ, 935, 110

Trump, J. R., Arrabal Haro, P., Simons, R. C., et al. 2023, ApJ, 935, 35

Trussler, J. A. A., Adams, N. J., Conselice, C. J., et al. 2022, arXiv:2207.14265

Ucci, G., Dayal, P., Hutter, A., et al. 2023, MNRAS, 518, 3557

Vanzella, E., Meneghetti, M., Caminha, G. B., et al. 2020, MNRAS, 494, L81

Wang, X., Cheng, C., Ge, J., et al. 2022, arXiv:2212.04476

Whitler, L., Stark, D. P., Endsley, R., et al. 2023, MNRAS, 519, 5859

Wilkins, S. M., Feng, Y., Di-Matteo, T., et al. 2016, MNRAS, 458, L6

Wilkins, S. M., Vijayan, A. P., Lovell, C. C., et al. 2023, MNRAS, 519, 3118

Wilkins, S. M., Vijayan, A. P., Lovell, C. C., et al. 2022, MNRAS, 517, 3227
Williams, H., Kelly, P. L., Chen, W., et al. 2023, Sci, 380, 416
Yan, H., Ma, Z., Ling, C., et al. 2023, ApJL, 942, L9
Yoon, I., Carilli, C. L., Fujimoto, S., et al. 2022, arXiv:2210.08413
Yung, L. Y. A., Somerville, R. S., Ferguson, H. C., et al. 2022, MNRAS, 515, 5416
Yung, L. Y. A., Somerville, R. S., Finkelstein, S. L., et al. 2020a, MNRAS, 496, 4574
Yung, L. Y. A., Somerville, R. S., Finkelstein, S. L., Popping, G., & Davé, R. 2019a, MNRAS, 483, 2983
Yung, L. Y. A., Somerville, R. S., Popping, G., et al. 2019b, MNRAS, 490, 2855
Yung, L. Y. A., Somerville, R. S., Popping, G., & Finkelstein, S. L. 2020b, MNRAS, 494, 1002
Zackrisson, E., Rydberg, C.-E., Schaerer, D., Östlin, G., & Tuli, M. 2011, ApJ, 740, 13